INTERNATIONAL JOURNAL FOR NUMERICAL METHODS IN ENGINEERING
Int. J. Numer. Meth. Engng 2006; **65**:190–223
Published online 1 September 2005 in Wiley InterScience (www.interscience.wiley.com). DOI: 10.1002/nme.1446

Multiscale modelling of particle debonding in reinforced elastomers subjected to finite deformations

Karel Matouš*,† and Philippe H. Geubelle‡

Center for Simulation of Advanced Rockets and Department of Aerospace Engineering, University of Illinois at Urbana-Champaign, Urbana, IL 61801, U.S.A.

SUMMARY

Interfacial damage nucleation and evolution in reinforced elastomers subjected to finite strains is modelled using the mathematical theory of homogenization based on the asymptotic expansion of unknown variables. The microscale is characterized by a periodic unit cell, which contains particles dispersed in a blend and the particle matrix interface is characterized by a cohesive law. A novel numerical framework based on the perturbed Petrov–Galerkin method for the treatment of nearly incompressible behaviour is employed to solve the resulting boundary value problem on the microscale and the deformation path of a macroscale particle is predefined as in the micro-history recovery procedure. A fully implicit and efficient finite element formulation, including consistent linearization, is presented. The proposed multiscale framework is capable of predicting the non-homogeneous micro-fields and damage nucleation and propagation along the particle matrix interface, as well as the macroscopic response and mechanical properties of the damaged continuum. Examples are considered involving simple unit cells in order to illustrate the multiscale algorithm and demonstrate the complexity of the underlying physical processes. Copyright © 2005 John Wiley & Sons, Ltd.

KEY WORDS: multiscale analysis; asymptotic homogenization; particulate composites; stabilized finite elements; cohesive model

1. INTRODUCTION

Since the pioneering work of Hill [1, 2] and Hashin and Shtrikman [3], it has been widely recognized that phenomena occurring at lower scales often have a major impact on the macroscopic behaviour of heterogeneous systems and that multiscale modelling may lead to more accurate predictions of the overall material response. A wide range of approaches has been

*Correspondence to: Karel Matouš, Center for Simulation of Advanced Rockets, University of Illinois at Urbana-Champaign, Urbana, IL 61801, U.S.A.
†E-mail: matous@uiuc.edu
‡E-mail: geubelle@uiuc.edu

Contract/grant sponsor: U.S. Department of Energy; contract/grant number: B341494

Received 10 February 2005
Revised 11 July 2005
Accepted 18 July 2005

proposed to achieve the link between macro- and micro-levels. Many coupling procedures are based on micromechanics [4, 5]. Advantages of such approaches include simple evaluation of the micro-level fields, easy data transfer and analytical description of the macroscopic behaviour. However, micromechanics-based methods usually rely on limiting assumptions (low particle volume fraction, simple constitutive models, etc.) that are needed to obtain closed-form constitutive formulas at the macroscale. Another class of multiscale approaches, based on Hill's averaging lemma and/or the mathematical theory of homogenization, links the deformation of the microstructure to the local deformation of the macro-continuum. In particular, the mathematical theory of homogenization, which uses an asymptotic expansion of displacement, strain and stress fields about macroscopic values, has been used by several researchers for analysing multiscale responses [6, 7]. Other recent models devoted to multiscale modelling of heterogeneous systems at small and finite strains are those of Michel *et al.* [8], Miehe *et al.* [9], Kouznetsova *et al.* [10] and Gosh *et al.* [11] to name just a few. An effective local-global technique based on the hierarchical decomposition of field variables has also been proposed by Garikipati and Hughes [12] while Strouboulis and co-workers [13] proposed a generalized finite element method using mesh-based handbook functions. Finally, Fish and Chen [14] have used the multigrid method for solving heterogeneous media with strong scale mixing.

In the present work, the damage nucleation and propagation along the particles matrix interfaces in particulate reinforced elastomers under finite strains are modelled using a multiscale analysis procedure within a cohesive finite element framework. Analysis of damage evolution in reinforced elastomers is quite complex, especially for those characterized by a high volume fraction of the reinforcing phase, such as solid propellants. In these highly filled elastomers, experimental observations have shown that the failure process is primarily driven by the debonding of the larger particles, with the smaller particles playing the role of stiffener for the matrix [15, 16].

The number and complexity of these phenomena have led most of the modelling efforts reported in the literature to rely on homogenized continuum models to capture some of these key features of the mechanical response. For example, Bergstrom and Boyce [17] have proposed a dual-network model to predict the non-linear viscoelastic response of carbon-black reinforced rubbers, with emphasis on capturing the large deformation and Mullins effects. Drozdov and Dorfmann [18] also used the network theory of rubber elasticity to capture the non-linear equilibrium response of filled and unfilled elastomers. Various homogenized models have been also proposed to simulate the damage evolution: see, for example, the analysis presented by Farris [19], Schapery [20], Ha and Schapery [21], Simo [22], Ravichandran and Liu [23]. Other approaches rely on micromechanics [5, 24, 25]. Most theories, however, are based on phenomenological continuum models of various features of the constitutive response of filled elastomers. Examples include Dorfmann and Ogden's analysis of the Mullins effect [26], Kaliske and Rothert's work on the internal friction [27] and Miehe and Keck's stress decomposition model of damage evolution [28].

Another complexity is associated with the numerical treatment of these materials. As mentioned earlier, the matrix material is nearly incompressible and a special numerical formulation has to be employed. A mixed finite element method that interpolates the pressure and displacement fields separately is required. For Galerkin methods, the choice of interpolation functions must satisfy the Babuška–Brezzi condition (see, e.g. Reference [29]) in order to achieve uniqueness, convergence and robustness. Without balancing the interpolations properly, significant oscillations in the solution typically result. Considerable effort has been devoted in

recent years to develop novel numerical techniques that give stable solution [30–32]. Especially, stabilized theories, where Babuška–Brezzi stability condition is circumvented, have been recently explored [33–35].

To achieve a better description of the microstructural damage process, Zhong and Knauss [36, 37] performed a cohesive finite element analysis of unit cell models to study the progressive decohesion of the particles. However, their analysis was performed in a 2D setting and did not involve a multiscale formulation and a consistent data transfer. Therefore, the macroscopic constitutive response presented in their work is likely to be strongly affected by the boundary conditions applied on the unit cell. Moreover, due to the numerical scheme used to solve the set of non-linear equations, the scope of their analysis was limited.

In this work, we build on Zhong and Knauss' preliminary investigation and perform a multiscale analysis where the microscale is characterized by a unit cell containing particles dispersed in a blend. The particle/matrix interface is modelled by a cohesive law describing the dewetting process in accordance to a prescribed traction-separation relation that accounts for mode mixity [38, 39]. However, unlike in Zhong and Knauss' study, we emphasize the link between the damage taking place at the particle level and the macroscopic constitutive response of the filled elastomer by adopting the mathematical theory of homogenization to couple the micro- and macro-domains. Moreover, a novel numerical solver is used to solve the resulting boundary value problem at the microscale in a fully 3D setting, and the micro-history recovery procedure by Fish *et al.* [40] is applied to describe the response of a material point at the macroscale.

In Section 2, we present the mathematical theory of homogenization based on an asymptotic expansion of unknown fields. Section 3 describes the cohesive model characterized by an exponential traction-separation law that accounts for mode mixity. A stabilized variational framework based on a Lagrangian formulation is presented in Section 4. The non-linear solver based on an arc-length procedure and consistent linearization are presented in Section 5. Section 6 describes constitutive laws characterizing the mechanical behaviour of individual constituents. We then present a set of examples involving simple unit cells to demonstrate the multiscale algorithm and complexity of the underlying physics (Section 7).

Adopting conventional symbolic notation practices, we herein denote second-order tensors with upper case boldface italic and lower case boldface Greek letters, e.g. $\boldsymbol{P}$ and $\boldsymbol{\sigma}$. The trace of a second-order tensor is denoted by $\mathrm{tr}(\boldsymbol{A})$, and the tensor operations between two second-order tensors $\boldsymbol{S}$ and $\boldsymbol{E}$ are indicated as $\boldsymbol{SE}$ for the tensor contraction (a second-order tensor) and $\boldsymbol{S} : \boldsymbol{E}$ for the scalar product (a double contraction). Other notational conventions adopted in this paper are introduced as needed.

2. MATHEMATICAL THEORY OF HOMOGENIZATION

We describe, in this section, the mathematical theory of homogenization in the finite strain setting. This theory was used successfully by several researchers, but has been primarily limited to small strain problems [6, 7]. Finite strain homogenization procedures, based on Hill's averaging lemma, have also been proposed [9, 10]. However, to our knowledge, the mathematical theory of homogenization that includes the cohesive zone modelling of interfacial damage evolution in heterogeneous solids subjected to finite deformations has not yet been proposed.

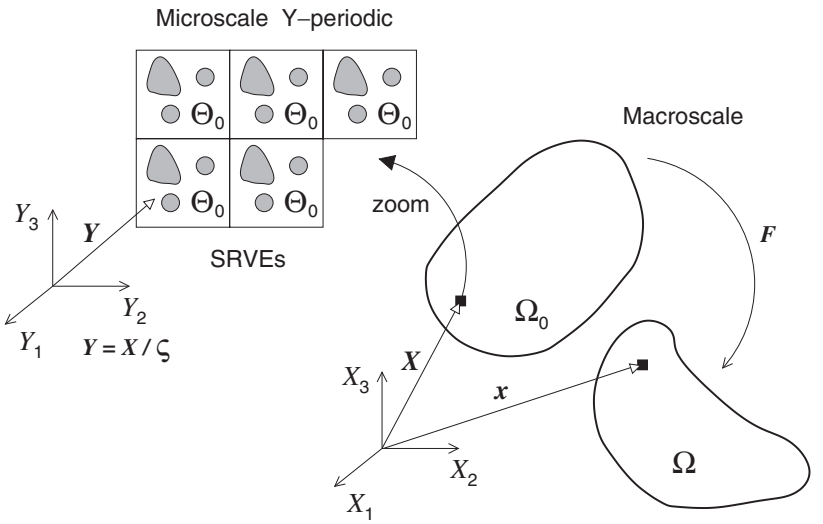

Figure 1. Kinematic decomposition of deformation gradients, and microscopic and macroscopic domains.

Let us consider a composite material composed of hyperelastic particles embedded in a hyperelastic matrix. The composite is assumed to be locally periodic (Y-periodic) with the period of microstructure defined by a statistically representative volume element (SRVE), denoted by Θ_0, as shown in Figure 1. This body undergoes the motion $\boldsymbol{\phi}(\boldsymbol{X}, \boldsymbol{Y})$, and $\boldsymbol{F}(\boldsymbol{X}, \boldsymbol{Y}) = \nabla\boldsymbol{\phi}(\boldsymbol{X}, \boldsymbol{Y})$ denotes the deformation gradient with the Jacobian given by $J = \det(\boldsymbol{F})$. Here $\boldsymbol{X} \in \mathbb{R}^3$ designates the position of a particle in the reference macroscopic configuration $\Omega_0 \subset \mathbb{R}^3$ in the Cartesian co-ordinate system. Next, consider $\boldsymbol{Y} = \boldsymbol{X}/\varsigma$ be the microscopic position vector in $\Theta_0 \subset \mathbb{R}^3$ in the Cartesian co-ordinate system. Henceforth, ς denotes a very small positive number that, roughly speaking, corresponds to the size of a microstructure; $\boldsymbol{X}$ and $\boldsymbol{Y}$ are referred to as *slow* and *fast* variables, respectively.

Next, let the heterogeneity be enclosed by a cohesive surface S_0 with a unit normal $\boldsymbol{N}_0$, and let $\boldsymbol{x} = \boldsymbol{\phi}(\boldsymbol{X}, \boldsymbol{Y})$ be the spatial co-ordinates of a particle, with $\boldsymbol{x} = \boldsymbol{X} + \boldsymbol{u}(\boldsymbol{X}, \boldsymbol{Y})$, where the displacement field $\boldsymbol{u}$ is approximated in terms of the double-scale asymptotic expansion on $\Omega \times \Theta$ as

$$\boldsymbol{u}(\boldsymbol{X}, \boldsymbol{Y}) \approx {}^0\boldsymbol{u}(\boldsymbol{X}, \boldsymbol{Y}) + \varsigma\,{}^1\boldsymbol{u}(\boldsymbol{X}, \boldsymbol{Y}) + \text{h.o.t.} \tag{1}$$

Here the left superscripts ${}^{0,1,\cdots}$ represent the asymptotic order. Using a Lagrangian formulation and employing the indirect macroscopic spatial derivatives, $\nabla_X(\boldsymbol{\phi}(\boldsymbol{X}, \boldsymbol{Y} = \boldsymbol{X}/\varsigma)) = \nabla_X\boldsymbol{\phi} + (1/\varsigma)\nabla_Y\boldsymbol{\phi}$, the deformation gradient reads

$$\boldsymbol{F} = \frac{\partial \boldsymbol{x}}{\partial \boldsymbol{X}} = \mathbf{1} + \nabla_X\boldsymbol{u} \approx \varsigma^{-1}\nabla_Y{}^0\boldsymbol{u} + \varsigma^0[\mathbf{1} + (\nabla_X{}^0\boldsymbol{u} + \nabla_Y{}^1\boldsymbol{u})] + \text{h.o.t.} \tag{2}$$

where $\mathbf{1}$ represents the second-order identity tensor. The higher-order terms h.o.t. $\equiv \varsigma^1(\nabla_X{}^1\boldsymbol{u} + \nabla_Y{}^2\boldsymbol{u}) + \varsigma^2(\cdots) + \cdots$ are not considered in this analysis. Thus, the deformation gradients for

the first two asymptotic orders ς^{-1} and ς^{0} are given by

$$\begin{aligned} {}^{(-1)}\boldsymbol{F} &= \nabla_Y {}^0\boldsymbol{u} \\ {}^{0}\boldsymbol{F} &= [\mathbf{1} + (\nabla_X {}^0\boldsymbol{u} + \nabla_Y {}^1\boldsymbol{u})] \end{aligned} \tag{3}$$

where ∇_X and ∇_Y denote gradients with respect to the $\boldsymbol{X}$ and $\boldsymbol{Y}$ co-ordinates, respectively.

The constitutive relations in terms of the first Piola–Kirchoff (P–K) stresses for various asymptotic orders ^{i} are given by

$${}^i\boldsymbol{P} = \left.\frac{\partial W}{\partial \boldsymbol{F}}\right| \boldsymbol{F} = {}^i\boldsymbol{F} \tag{4}$$

and the resulting asymptotic expansion of the stress field yields

$$\boldsymbol{P}(\boldsymbol{X}, \boldsymbol{Y}) \approx \varsigma^{-1\,(-1)}\boldsymbol{P} + \varsigma^{0\,(0)}\boldsymbol{P} + \cdots \tag{5}$$

where a free energy density function, W, is introduced in Section 6.

Described in terms of the reference configuration, the governing equations, including the contribution of the cohesive zone, are

$$\begin{aligned} \nabla \cdot \boldsymbol{P} + \boldsymbol{f} &= \mathbf{0} \quad \text{in } \Omega_0 \\ \boldsymbol{P} \cdot \boldsymbol{N} &= \underline{\boldsymbol{t}} \quad \text{on } \boldsymbol{\phi}(\partial\Omega_{\boldsymbol{P}}) \\ \boldsymbol{u} &= \bar{\boldsymbol{u}} \quad \text{on } \boldsymbol{\phi}(\partial\Omega_{\boldsymbol{u}}) \\ \lfloor \boldsymbol{P} \cdot \boldsymbol{N}_0 \rceil \equiv \lfloor \boldsymbol{t}_0 \rceil &= \mathbf{0} \quad \text{on } S_0 \end{aligned} \tag{6}$$

where $\boldsymbol{t}_0$ represents the cohesive tractions across S_0, $\boldsymbol{f}(\boldsymbol{X}, \boldsymbol{Y})$ denotes body forces and $\underline{\boldsymbol{t}}(\boldsymbol{X})$ represents prescribed macroscopic tractions on the boundary $\boldsymbol{\phi}(\partial\Omega_{\boldsymbol{P}})$. We also consider Dirichlet boundary conditions $\bar{\boldsymbol{u}}$ on $\boldsymbol{\phi}(\partial\Omega_{\boldsymbol{u}})$. Moreover, the symbol $\lfloor \bullet \rceil = (\bullet^+ - \bullet^-)$ denotes the jump of a quantity $\bullet$ across the cohesive surface and $^{\pm}$ represents plus and minus sides of the cohesive surface, $S_0^{\pm}$.

Following standard variational methods, the principle of virtual work reads

$$\int_{\Omega_0} \boldsymbol{P} : \nabla \delta\boldsymbol{u} \, \mathrm{d}\Omega_0 + \int_{S_0} \boldsymbol{t}_0 \cdot \lfloor \delta\boldsymbol{u} \rceil \, \mathrm{d}S_0 - \int_{\Omega_0} \boldsymbol{f} \cdot \delta\boldsymbol{u} \, \mathrm{d}\Omega_0 - \int_{\partial\Omega_0} \underline{\boldsymbol{t}} \cdot \delta\boldsymbol{u} \, \mathrm{d}A_0 = 0 \tag{7}$$

for all admissible variations $\delta\boldsymbol{u}$ satisfying

$$\delta\boldsymbol{u} \in \mathfrak{U} \subset [H^1]^{\mathfrak{N}}, \quad \delta\boldsymbol{u} = \mathbf{0} \quad \text{on } \boldsymbol{\phi}(\partial\Omega_{\boldsymbol{u}}) \tag{8}$$

where $\mathfrak{N}$ is the space dimension and H^1 represents the Sobolev space.

As apparent in (7), the presence of a cohesive surface results in an additional term in the principle of virtual work, which can be deduced from the unbounded part of the gradient of the weighting function [41]. Note, however, that in this work, the discontinuity is always contained between volumetric elements as opposed to the generalized finite elements methods [41]. Hence, the test functions lie in the space of bounded variations since they are discontinuous across the interface. The cohesive tractions perform work on the displacement jumps or

'opening displacements' over the cohesive surface:

$$\boldsymbol{\chi} \equiv \lfloor \boldsymbol{\phi}(\boldsymbol{X}, \boldsymbol{Y}) \rceil = \lfloor \boldsymbol{u} \rceil \tag{9}$$

The detailed derivation of the cohesive part is presented in Section 3.

Introducing the asymptotic expansions (1) and (5) into (7), taking the limit when $\varsigma \to 0^+$ and making use of the indirect spatial derivatives, the principle of the virtual work (7) holds in the terms of the same power of ς,

$$\mathcal{O}(\varsigma^{-2}) : \frac{1}{|\Theta_0|} \int_{\Omega_0} \int_{\Theta_0} {}^{(-1)}\boldsymbol{P} : \nabla_Y \delta\boldsymbol{u} \, \mathrm{d}\Theta_0 \, \mathrm{d}\Omega_0 = 0 \tag{10a}$$

$$\mathcal{O}(\varsigma^{-1}) : \frac{1}{|\Theta_0|} \int_{\Omega_0} \int_{\Theta_0} [{}^{(-1)}\boldsymbol{P} : \nabla_X \delta\boldsymbol{u} + {}^{0}\boldsymbol{P} : \nabla_Y \delta\boldsymbol{u}] \, \mathrm{d}\Theta_0 \, \mathrm{d}\Omega_0 + \frac{1}{|\Theta_0|} \int_{\Omega_0} \int_{S_0} \boldsymbol{t}_0 \cdot \lfloor \delta\boldsymbol{u} \rceil \, \mathrm{d}S_0 \, \mathrm{d}\Omega_0 = 0 \tag{10b}$$

$$\mathcal{O}(\varsigma^{0}) : \frac{1}{|\Theta_0|} \int_{\Omega_0} \int_{\Theta_0} {}^{0}\boldsymbol{P} : \nabla_X \delta\boldsymbol{u} \, \mathrm{d}\Theta_0 \, \mathrm{d}\Omega_0 - \frac{1}{|\Theta_0|} \int_{\Omega_0} \int_{\Theta_0} \boldsymbol{f} \cdot \delta\boldsymbol{u} \, \mathrm{d}\Theta_0 \, \mathrm{d}\Omega_0 - \int_{\partial\Omega_0} \underline{\boldsymbol{t}} \cdot \delta\boldsymbol{u} \, \mathrm{d}A_0 = 0 \tag{10c}$$

for all $\delta\boldsymbol{u} \in V_{\Omega\times\Theta}$, where

$$V_{\Omega\times\Theta} = \{\delta\boldsymbol{u}(\boldsymbol{X}, \boldsymbol{Y}) \mid \delta\boldsymbol{u}(\boldsymbol{X}, \boldsymbol{Y}) \in \Omega \times \Theta, \ \ \delta\boldsymbol{u}(\bullet, \boldsymbol{Y}) \text{ is } Y\text{-periodic}, \ \ \delta\boldsymbol{u}|_{\partial\Omega_u} = \boldsymbol{0}\} \tag{11}$$

Note that the following integration rules have been applied:

$$\begin{aligned} \lim_{\varsigma\to 0^+} \int_{\Omega_0} \bullet(\boldsymbol{X}/\varsigma) \, \mathrm{d}\Omega_0 &= \frac{1}{|\Theta_0|} \int_{\Omega_0} \int_{\Theta_0} \bullet(\boldsymbol{Y}) \, \mathrm{d}\Theta_0 \, \mathrm{d}\Omega_0 \\ \lim_{\varsigma\to 0^+} \varsigma \int_{S_0} \bullet(\boldsymbol{X}/\varsigma) \, \mathrm{d}S_0 &= \frac{1}{|\Theta_0|} \int_{\Omega_0} \int_{S_0} \bullet(\boldsymbol{Y}) \, \mathrm{d}S_0 \, \mathrm{d}\Omega_0 \end{aligned} \tag{12}$$

to integrate the Y-periodic function $\bullet$ [7].

Let us first consider the $\mathcal{O}(\varsigma^{-2})$ equation (10a). Since the variation of the displacement field $\delta\boldsymbol{u}$ is an arbitrary, one can choose $\delta\boldsymbol{u} = \delta\boldsymbol{u}(\boldsymbol{Y})$. Then, integrating by parts, applying the divergence theorem and noting that the terms on the opposite faces of the unit cell cancel due to the periodicity condition, we obtain

$$\nabla_Y \cdot {}^{(-1)}\boldsymbol{P} = \boldsymbol{0} \quad \text{and} \quad {}^{0}\boldsymbol{u} = {}^{0}\boldsymbol{u}(\boldsymbol{X}) \quad \Rightarrow \quad {}^{(-1)}\boldsymbol{F} = {}^{(-1)}\boldsymbol{P} = \boldsymbol{0} \tag{13}$$

The deformation gradient (2) and displacement jump (9) across the cohesive surface can now be rewritten as

$$\begin{aligned} \boldsymbol{F} &\approx [\boldsymbol{1} + \nabla_X {}^{0}\boldsymbol{u}] + \nabla_Y {}^{1}\boldsymbol{u} = \underline{\boldsymbol{F}} + \nabla_Y {}^{1}\boldsymbol{u} \\ \boldsymbol{\chi} &\equiv \lfloor \boldsymbol{u} \rceil = \lfloor {}^{1}\boldsymbol{u} \rceil \end{aligned} \tag{14}$$

where $\underline{\boldsymbol{F}} = [\mathbf{1} + \nabla_X {}^0\boldsymbol{u}]$ denotes the macroscopic deformation gradient and $\nabla_Y {}^1\boldsymbol{u}$ represents the gradient of the fluctuation microscopic displacement field. Here and henceforth, a quantity marked by an underline $\underline{\bullet}$ denotes a quantity $\bullet$ at the macroscale.

Focusing on one macroscopic material point and choosing $\delta\boldsymbol{u} = \delta^1\boldsymbol{u}$, the $\mathcal{O}(\varsigma^{-1})$ equation

$$\frac{1}{|\Theta_0|}\int_{\Theta_0} {}^0\boldsymbol{P} : \nabla_Y \delta^1\boldsymbol{u}\,\mathrm{d}\Theta_0 + \frac{1}{|\Theta_0|}\int_{S_0} \boldsymbol{t}_0 \cdot \lfloor \delta^1\boldsymbol{u} \rceil\,\mathrm{d}S_0 = 0 \tag{15}$$

with

$${}^1\boldsymbol{u} = Y\text{-periodic} \quad \text{on } \boldsymbol{\phi}(\partial\Theta) \quad \text{and} \quad \delta^1\boldsymbol{u} \in \mathfrak{U}, \quad \delta^1\boldsymbol{u} = \mathbf{0} \quad \text{on } \boldsymbol{\phi}(\partial\Theta) \tag{16}$$

represents the weak form of the equilibrium at the microscale for purely kinematic boundary conditions. In addition, due to the periodicity assumption and in order to satisfy the equilibrium with the neighbouring SRVEs, the tractions on the SRVE boundary, $\partial\Theta_0$, will also be periodic. The computational approach for solving (15) is described in Sections 4 and 5.

Finally, the $\mathcal{O}(\varsigma^0)$ equation with $\delta\boldsymbol{u} = \delta^0\boldsymbol{u}$ denotes the weak form of the equilibrium equation at the macroscale

$$\int_{\Omega_0} \underline{\boldsymbol{P}} : \nabla\delta^0\boldsymbol{u}\,\mathrm{d}\Omega_0 - \int_{\Omega_0} \underline{\boldsymbol{f}} \cdot \delta^0\boldsymbol{u}\,\mathrm{d}\Omega_0 - \int_{\partial\Omega_0} \underline{\boldsymbol{t}} \cdot \delta^0\boldsymbol{u}\,\mathrm{d}A_0 = 0 \tag{17}$$

where the macroscopic first P–K stress and the macroscopic body force are defined as

$$\begin{aligned} \underline{\boldsymbol{P}} &= \frac{1}{|\Theta_0|}\int_{\Theta_0} {}^0\boldsymbol{P}\,\mathrm{d}\Theta_0 \\ \underline{\boldsymbol{f}} &= \frac{1}{|\Theta_0|}\int_{\Theta_0} \boldsymbol{f}\,\mathrm{d}\Theta_0 \end{aligned} \tag{18}$$

with

$${}^0\boldsymbol{u} = \bar{\boldsymbol{u}} \quad \text{on } \boldsymbol{\phi}(\partial\Omega_{\boldsymbol{u}}) \quad \text{and} \quad \delta^0\boldsymbol{u} \in \mathfrak{U}, \quad \delta^0\boldsymbol{u} = \mathbf{0} \quad \text{on } \boldsymbol{\phi}(\partial\Omega_{\boldsymbol{u}}) \tag{19}$$

In other words, the volume average of the variation of the work performed on the SRVE equals the local variation of the work at the macroscale, and the microscale fluctuation field does not contribute to the average variation of the work. The macroscopic boundary value problem is not solved numerically in this work. The deformation path of a macroscale material point is rather predefined as in the micro-history recovery procedure by Fish *et al.* [40]. For a more detailed description of the mathematical theory of homogenization in a small strain setting, see References [6, 7, 40].

3. FINITE STRAIN IRREVERSIBLE COHESIVE LAW

Here we describe the finite strain irreversible cohesive law introduced in Equations (6) and (7) and subsequently in the boundary value problem at the microscale (Equation (15)). Let us recall that the displacement jump, Equation (9), is reduced by Equation (14) to

$$\boldsymbol{\chi} \equiv \lfloor \boldsymbol{\phi}(\boldsymbol{X}, \boldsymbol{Y}) \rceil \equiv \lfloor \boldsymbol{u} \rceil = \lfloor {}^1\boldsymbol{u} \rceil \tag{20}$$

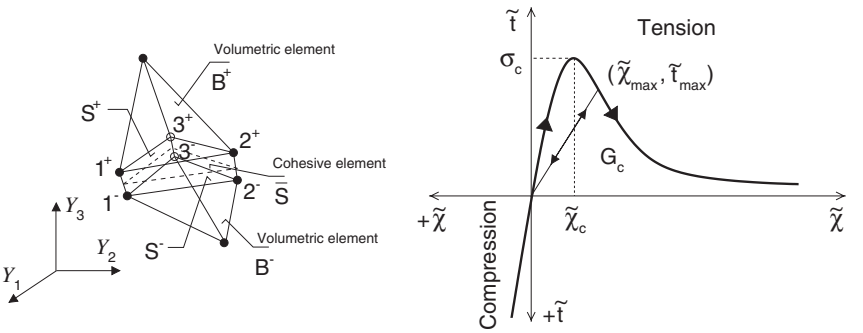

Figure 2. Geometry of cohesive element and irreversible cohesive law.

Please note that $\boldsymbol{\chi}$ vanishes identically when the body undergoes a rigid transformation, as required of a proper deformation measure. The cohesive element is shown schematically in Figure 2 together with the effective traction-separation law, which is described in what follows.

By recourse to Coleman and Noll's method [42, 43], it is possible to show that the local tractions $\boldsymbol{t}_0$ take the form

$$\boldsymbol{t}_0 = \frac{\partial \psi}{\partial \boldsymbol{\chi}} \tag{21}$$

It is worth noting in this regard that the cohesive free energy ψ is subject to the restrictions imposed by material frame indifference. Following the approach proposed by Ortiz and Pandolfi [39], the unique deformed cohesive surface $\bar{S}$ is defined in terms of the mean deformation mapping

$$\bar{\boldsymbol{\phi}}(\boldsymbol{X}, \boldsymbol{Y}) = \tfrac{1}{2}[\boldsymbol{\phi}^{+}(\boldsymbol{X}, \boldsymbol{Y}) + \boldsymbol{\phi}^{-}(\boldsymbol{X}, \boldsymbol{Y})], \quad \boldsymbol{\phi}^{\pm}(\boldsymbol{X}, \boldsymbol{Y}) = \bar{\boldsymbol{\phi}}(\boldsymbol{X}, \boldsymbol{Y}) \pm \tfrac{1}{2}\boldsymbol{\chi} \tag{22}$$

and the traction separation law is given by

$$\boldsymbol{t}_0 = \frac{\tilde{t}}{\tilde{\chi}}\,\hat{\boldsymbol{t}}, \quad \hat{\boldsymbol{t}} = [\beta^2 \boldsymbol{\chi} + (1 - \beta^2)(\boldsymbol{\chi} \cdot \boldsymbol{N})\boldsymbol{N}] \tag{23}$$

where β assigns different weights to the sliding and normal opening displacements and $\boldsymbol{N}$ denotes the unit normal of the cohesive surface $\bar{S}$ in the current configuration.

The present work adopts the simple and computationally convenient cohesive law [39, 44, 45] (Figure 2)

$$\psi = \mathrm{e}\sigma_{\mathrm{c}}\chi_{\mathrm{c}}\left[1 - \left(1 + \frac{\tilde{\chi}}{\chi_{\mathrm{c}}}\right)\mathrm{e}^{-\tilde{\chi}/\chi_{\mathrm{c}}}\right] \tag{24a}$$

$$\tilde{t} = \frac{\partial \psi}{\partial \tilde{\chi}} = \mathrm{e}\sigma_{\mathrm{c}}\,\frac{\tilde{\chi}}{\chi_{\mathrm{c}}}\,\mathrm{e}^{-\tilde{\chi}/\chi_{\mathrm{c}}} \tag{24b}$$

where $\mathrm{e} = \exp(1)$, χ_c denotes the characteristic opening displacement and σ_c is the maximum effective cohesive traction. The effective opening displacement $\tilde{\chi}$ is defined by

$$\tilde{\chi} = \sqrt{\beta^2 \tilde{\chi}_s^2 + \tilde{\chi}_\mathrm{n}^2} \tag{25}$$

while the normal and tangential displacement jump components are

$$\tilde{\chi}_\mathrm{n} = \boldsymbol{\chi} \cdot \boldsymbol{N}, \quad \tilde{\chi}_s = |\boldsymbol{\chi}_s|, \quad \boldsymbol{\chi}_s = (\mathbf{1} - \boldsymbol{N} \otimes \boldsymbol{N})\boldsymbol{\chi} \tag{26}$$

where $\otimes$ denotes dyadic product. As in Reference [39], we shall assume loading if $\tilde{\chi} = \tilde{\chi}_{\max}$ and $\dot{\tilde{\chi}} \geqslant 0$. The evolution of the internal state variable, $\tilde{\chi}_{\max}$, is given by

$$\dot{\tilde{\chi}}_{\max} = \begin{cases} \dot{\tilde{\chi}} & \text{if } \tilde{\chi} = \tilde{\chi}_{\max} \quad \text{and} \quad \dot{\tilde{\chi}} \geqslant 0 \\ 0 & \text{otherwise} \end{cases} \tag{27}$$

We also assume unloading to be directed towards the origin (Figure 2), giving

$$\tilde{t} = \frac{\tilde{t}_{\max}}{\tilde{\chi}_{\max}} \tilde{\chi} \quad \text{if } \tilde{\chi} < \tilde{\chi}_{\max} \quad \text{or } \dot{\tilde{\chi}} < 0 \tag{28}$$

For the cohesive model described by (24), the cohesive fracture energy per unit area of the cohesive surface is given by

$$G_\mathrm{c} = \int_0^\infty \tilde{t}\, \mathrm{d}\tilde{\chi} = \mathrm{e}\sigma_\mathrm{c}\chi_\mathrm{c} \tag{29}$$

It bears emphasis that, upon closure, the cohesive surfaces are subjected to a (possibly frictional) contact constraint. Instead of a more complex numerical treatment of the contact between the crack faces, such as in Reference [46], we enforce the contact constraint with the aid of a non-sliding (stick) exponentially increasing compressive constraint on the effective cohesive traction (Figure 2):

$$\tilde{t} = \tilde{\chi}\sigma_\mathrm{c} \frac{\tilde{\chi} + \chi_\mathrm{c}}{\chi_\mathrm{c}^2} \mathrm{e}^{(\tilde{\chi}+\chi_\mathrm{c}/\chi_\mathrm{c})} \quad \forall \tilde{\chi} > 0 \quad \text{if } \tilde{\chi}_\mathrm{n} < 0 \tag{30}$$

Please note that the effective opening displacement and effective tractions are always positive, that contact is detected for negative normal opening displacement, $\tilde{\chi}_\mathrm{n} < 0$, and that the first derivatives of (24b) and (30) evaluated at $\tilde{\chi} = 0$ are identical.

4. STABILIZED FINITE ELEMENT FORMULATION

We now outline the variational formulation and numerical treatment by the finite element method of the elliptic boundary value problem of the micro-continuum ($\mathcal{O}(\varsigma^{-1})$, Equation 15), with special emphasis on the derivation of a consistent linearization of the non-linear problem and on the accurate numerical treatment of the near-incompressible response of a matrix.

On the latter issue, the present finite element procedure is based on a stabilized Petrov–Galerkin formulation to treat volume constraints arising from the nearly incompressible

hyperelastic material behaviour. Employing the additive decomposition of the free energy density into distortional and volumetric components

$$W(\boldsymbol{C}) = \hat{W}(\boldsymbol{C}) + U(J) \tag{31}$$

the second P–K tensor in the reference configuration is obtained in the standard manner:

$$\begin{aligned} \boldsymbol{S} &= 2\,\frac{\partial \hat{W}}{\partial \boldsymbol{C}} + \gamma J \boldsymbol{C}^{-1} \\ \gamma &= \frac{\mathrm{d}U}{\mathrm{d}J} \end{aligned} \tag{32}$$

where $\boldsymbol{C} = \boldsymbol{F}^{\mathrm{T}}\boldsymbol{F}$ denotes the Cauchy–Green deformation tensor. Note that the scalar multiplier γ is equal to the hydrostatic stress 'pressure', $\gamma \equiv p = 1/3\,\mathrm{tr}(\boldsymbol{\sigma})$, only if the energy density is a homogeneous function of zeroth order [47]. We can therefore express the energy function W in terms of the distortional component of the right Cauchy–Green tensor $\hat{\boldsymbol{C}} = (\det \boldsymbol{C})^{-1/3}\boldsymbol{C}$ to give a formally modified energy functional $\hat{W}(\boldsymbol{C}) = W(\hat{\boldsymbol{C}})$. Details of this substitution are derived in Reference [47] and the same approach was used by Klaas *et al.* [34]. As expected, the first and second P–K stresses defined on Θ_0 are related by $\boldsymbol{P} = \boldsymbol{F}\boldsymbol{S}$. In this work, we use the following simple expression for the volumetric function $U(J)$:

$$\begin{aligned} U(J) &= \tfrac{1}{2}\kappa(J-1)^2 \\ p &= \kappa(J-1) \end{aligned} \tag{33}$$

where κ is the bulk modulus. Note that the asymptotic order ^{0} was dropped from the equations since $\boldsymbol{F} = {}^0\boldsymbol{F} + \mathcal{O}(\varsigma)$ and $\boldsymbol{P} = {}^0\boldsymbol{P} + \mathcal{O}(\varsigma)$ and only the first term of the asymptotic expansion is considered. The distortional component of a free energy density function is introduced in Section 6.

As described by Klaas *et al.* [34], mesh-dependent terms that are functions of the Euler–Lagrange equations from finer scale are added to the variational statement (15) and the pressure p is interpolated as an independent variable. In particular, the push-forward of the gradient of pressure weighting function, $\boldsymbol{F}^{-\mathrm{T}}\nabla\delta p$, is used to perturb the Galerkin weighting space. Thus, the strong form of equilibrium equations is integrated with the weighting function

$$\delta\boldsymbol{v} = \delta^1\boldsymbol{u} + \Lambda\boldsymbol{F}^{-\mathrm{T}}\nabla\delta p \tag{34}$$

where the perturbation is applied elementwise and Λ is chosen following Hughes *et al.* [33] as

$$\Lambda = \frac{\omega h_{\mathrm{e}}^2}{2\mu} \tag{35}$$

Here, h_{e} denotes the characteristic element length, μ represents the shear modulus of the material and ω is a non-dimensional, non-negative stability parameter.

Using the standard variational procedure, inserting (32) into (15), taking into account (34) and enforcing (33) in a weak sense, we obtain the following stabilized mixed formulation

of the microscopic problem:

$$\mathscr{R}_{\boldsymbol{u}} \equiv \frac{1}{|\Theta_0|}\int_{\Theta_0} \tilde{\boldsymbol{S}} : (\boldsymbol{F}^{\mathrm{T}}\nabla\delta^1\boldsymbol{u})\,\mathrm{d}\Theta_0 + \frac{1}{|\Theta_0|}\int_{\Theta_0} Jp\boldsymbol{F}^{-\mathrm{T}} : (\nabla\delta^1\boldsymbol{u})\,\mathrm{d}\Theta_0 + \frac{1}{|\Theta_0|}\int_{S_0} \boldsymbol{t}_0 \cdot \lfloor\delta^1\boldsymbol{u}\rceil\,\mathrm{d}S_0 = 0 \tag{36a}$$

$$\mathscr{R}_p \equiv \frac{1}{|\Theta_0|}\int_{\Theta_0}\left[(J-1) - \frac{p}{\kappa}\right]\delta p\,\mathrm{d}\Theta_0 - \frac{1}{|\Theta_0|}\sum_{\mathrm{el}}^{\mathrm{ne}}\Lambda\int_{\Theta_0^e} J(\boldsymbol{F}^{-1}\boldsymbol{F}^{-\mathrm{T}}) : (\nabla p\otimes\nabla\delta p)\,\mathrm{d}\Theta_0^e + \frac{1}{|\Theta_0|}\sum_{\mathrm{el}}^{\mathrm{ne}}\Lambda\int_{\Theta_0^e} \underbrace{(\nabla\cdot[\boldsymbol{F}\tilde{\boldsymbol{S}}])}_{=0 \text{ for } P_1/P_1 \text{ elements}} \cdot(\boldsymbol{F}^{-\mathrm{T}}\nabla\delta p)\,\mathrm{d}\Theta_0^e = 0 \tag{36b}$$

where $\tilde{\boldsymbol{S}}$ represents the deviatoric part of $\boldsymbol{S}$, ne denotes the number of elements and $\delta^1\boldsymbol{u}$ and δp are arbitrary functions satisfying

$$\begin{aligned} &\delta^1\boldsymbol{u} \in \mathfrak{U}, \quad \delta^1\boldsymbol{u} = \boldsymbol{0} \quad \text{on } \boldsymbol{\phi}(\partial\Theta) \quad \text{and} \quad {}^1\boldsymbol{u} = Y\text{-periodic} \quad \text{on } \boldsymbol{\phi}(\partial\Theta) \\ &\delta p \in L_2 \end{aligned} \tag{37}$$

In particular, equal-order interpolations for the displacement and pressure (e.g. P_1/P_1) are supported by the present formulation. Due to the linear interpolation of the displacement field, the last term in (36b) is zero. For a more detailed description of mixed and stabilized formulations, see References [30, 32, 34].

It should be noted that the periodicity conditions are considered as constraints imposed to the discrete unknowns in the finite element solution procedure. Such conditions are simply fulfilled by assigning the same deformation identification numbers to the corresponding degrees of freedom related to the nodes on opposite sides of the unit cell. However, this requires that the mesh as well as the microstructure have the appropriate periodicity. Moreover, the corners of the unit cell are all associated with the same point and are thus fully prescribed.

The finite element method is combined with an arc-length procedure to solve the non-linear system of equations described by (36). The formulation of a consistent tangent stiffness tensor is thus essential to maintain a quadratic rate of convergence [48], if one is to employ a Newton's-type algorithm to solve the system of non-linear equations. The linearization procedure and the non-linear solver are presented in the next section.

5. NON-LINEAR SOLVER AND LOAD STEPPING PROCEDURE

In this work, the macroscopic deformation history, $\underline{\boldsymbol{F}}$, is applied to the unit cell with the loading parameterized by a scalar load multiplier, λ, as

$$\underline{\boldsymbol{F}} = \underline{\boldsymbol{F}}(\lambda) \quad \Rightarrow \quad \boldsymbol{F} = \underline{\boldsymbol{F}}(\lambda) + \nabla_Y\,{}^1\boldsymbol{u} \tag{38}$$

The system of non-linear equations (36) thus yields

$$\begin{aligned} \mathscr{R}_{\boldsymbol{u}}(\underline{\boldsymbol{F}}(\lambda), {}^1\boldsymbol{u}, p) &= 0 \\ \mathscr{R}_p(\underline{\boldsymbol{F}}(\lambda), {}^1\boldsymbol{u}, p) &= 0 \end{aligned} \tag{39}$$

The arc-length procedure [46] is used to solve the above system for the unknown displacement ${}^1\boldsymbol{u}$, pressure p and the load multiplier λ. The *linearized* form of the system of equations is then given by

$$\begin{aligned} \mathscr{R}_{\boldsymbol{u}} + D\mathscr{R}_{\boldsymbol{u}}[\Delta\lambda] + D\mathscr{R}_{\boldsymbol{u}}[\Delta^1\boldsymbol{u}] + D\mathscr{R}_{\boldsymbol{u}}[\Delta p] &= 0 \\ \mathscr{R}_p + D\mathscr{R}_p[\Delta\lambda] + D\mathscr{R}_p[\Delta^1\boldsymbol{u}] + D\mathscr{R}_p[\Delta p] &= 0 \end{aligned} \tag{40}$$

and the arc-length constraint can be written as

$$\Delta\boldsymbol{r} \cdot \Delta\boldsymbol{r} + \Delta\lambda^2 = \Delta l^2, \quad \Delta\boldsymbol{r} = [\Delta^1\boldsymbol{u}, \Delta p] \tag{41}$$

where Δl is a prescribed incremental arc length. Here, the linearized terms $D\mathscr{R}_{\boldsymbol{u}}[\Delta\lambda]$ and $D\mathscr{R}_p[\Delta\lambda]$ denote the forcing (load) components. The notation $\mathscr{R}_{\boldsymbol{y}}^{k+1} \approx \mathscr{R}_{\boldsymbol{y}}^k + D\mathscr{R}_{\boldsymbol{y}}[\Delta\boldsymbol{y}] = \boldsymbol{0}$ is employed in this paper for the consistent linearization of a non-linear system $\mathscr{R}_{\boldsymbol{y}} = \boldsymbol{0}$.

5.1. Consistent linearization about $({}^1\boldsymbol{u}, p)$

A consistent linearization for the set of non-linear equations about a configuration $({}^1\boldsymbol{u}, p)$ yields

$$\begin{aligned} D\mathscr{R}_{\boldsymbol{u}}[\Delta^1\boldsymbol{u}] = \frac{1}{|\Theta_0|}\int_{\Theta_0} \Bigg\{ & \underbrace{[\boldsymbol{F}^{\mathrm{T}}(\nabla\delta^1\boldsymbol{u})] : \mathscr{L} : [\nabla(\Delta^1\boldsymbol{u})]}_{\text{material contribution}} + \underbrace{[(\nabla\delta^1\boldsymbol{u})^{\mathrm{T}}\nabla(\Delta^1\boldsymbol{u})] : \tilde{\boldsymbol{S}}}_{\text{geometric contribution}} \\ & + \underbrace{pJ[\mathrm{tr}(\boldsymbol{F}^{-1}\nabla(\Delta^1\boldsymbol{u}))\mathrm{tr}(\boldsymbol{F}^{-1}\nabla\delta^1\boldsymbol{u}) - \mathrm{tr}(\boldsymbol{F}^{-1}\nabla(\Delta^1\boldsymbol{u})\boldsymbol{F}^{-1}\nabla\delta^1\boldsymbol{u})]}_{\text{pressure geometric contribution}} \Bigg\} \mathrm{d}\Theta_0 \\ & + \frac{1}{|\Theta_0|}\int_{S_0} \underbrace{D\boldsymbol{t}_0[\Delta^1\boldsymbol{u}^{\pm}] \cdot \lfloor\delta^1\boldsymbol{u}\rceil}_{\text{cohesive model contribution}} \mathrm{d}S_0 \end{aligned} \tag{42a}$$

$$D\mathscr{R}_{\boldsymbol{u}}[\Delta p] = \frac{1}{|\Theta_0|}\int_{\Theta_0} J\,\mathrm{tr}(\boldsymbol{F}^{-1}\nabla\delta^1\boldsymbol{u})\Delta p\,\mathrm{d}\Theta_0 \tag{42b}$$

$$\begin{aligned} D\mathscr{R}_p[\Delta^1\boldsymbol{u}] = \frac{1}{|\Theta_0|}\int_{\Theta_0} J\,\mathrm{tr}(\boldsymbol{F}^{-1}\nabla(\Delta^1\boldsymbol{u}))\delta p\,\mathrm{d}\Theta_0 - \frac{1}{|\Theta_0|}\sum_{\mathrm{el}}^{\mathrm{ne}}\Lambda\int_{\Theta_0^e} J[\mathrm{tr}(\boldsymbol{F}^{-1}\nabla(\Delta^1\boldsymbol{u}))\boldsymbol{C}^{-1} \\ -\boldsymbol{F}^{-1}\nabla(\Delta^1\boldsymbol{u})\boldsymbol{C}^{-1} - \boldsymbol{C}^{-1}(\nabla(\Delta^1\boldsymbol{u}))^{\mathrm{T}}\boldsymbol{F}^{-\mathrm{T}}] : [\nabla p \otimes \nabla\delta p]\,\mathrm{d}\Theta_0^e \end{aligned} \tag{42c}$$

$$D\mathscr{R}_p[\Delta p] = -\frac{1}{|\Theta_0|}\int_{\Theta_0}\frac{1}{\kappa}\,\delta p \Delta p\,\mathrm{d}\Theta_0$$

$$-\frac{1}{|\Theta_0|}\sum_{\mathrm{el}}^{\mathrm{ne}}\Lambda\int_{\Theta_0^e} J[\boldsymbol{F}^{-1}\boldsymbol{F}^{-\mathrm{T}}]:[\nabla(\Delta p)\otimes\nabla\delta p]\,\mathrm{d}\Theta_0^e \tag{42d}$$

with the tangent hyperelastic pseudo-moduli given by

$$\mathscr{L} = 2\frac{\partial\tilde{\boldsymbol{S}}}{\partial\boldsymbol{C}}\mathscr{A} = \mathscr{C}\mathscr{A} \tag{43}$$

Here we use the notation $\mathscr{A}$ for the fourth-order tensor $1/2(\partial\boldsymbol{C}/\partial\boldsymbol{F})$. The deviatoric part of the material stiffness tensor $\mathscr{C} = 2\partial\tilde{\boldsymbol{S}}/\partial\boldsymbol{C}$ is derived for a particular free density function in Section 6. The resulting tangent stiffness tensor is non-symmetric in the present analysis. Several finite element approximation schemes can be used within the proposed variational framework provided by (36). In this work, continuous displacement and pressure interpolations are assumed, i.e. we use the so-called P_1/P_1 elements. The system of linear equations (40) is solved using the sparse direct solver UMFPACK [49]. The consistent linearization of the cohesive model contribution, $D\boldsymbol{t}_0[\Delta^1\boldsymbol{u}^{\pm}]$, present in (42a), is described next.

5.2. Consistent linearization of cohesive model contribution

Let us first recall that the cohesive surface contribution in the principle of the virtual work is

$$\frac{1}{|\Theta_0|}\int_{S_0}\boldsymbol{t}_0\cdot\lfloor\delta^1\boldsymbol{u}\rceil\,\mathrm{d}S_0 \equiv \frac{1}{|\Theta_0|}\int_{S_0}\frac{\tilde{t}}{\tilde{\chi}}\hat{\boldsymbol{t}}\cdot\lfloor\delta^1\boldsymbol{u}\rceil\,\mathrm{d}S_0 \tag{44}$$

with the displacement jump and its weighting function defined by

$$\boldsymbol{\chi} = ({}^1\boldsymbol{u}^+ - {}^1\boldsymbol{u}^-) \tag{45a}$$

$$\lfloor\delta^1\boldsymbol{u}\rceil \equiv \delta^1\boldsymbol{u}^+ - \delta^1\boldsymbol{u}^- \tag{45b}$$

In addition, we recall that the cohesive tractions $\boldsymbol{t}_0$ are dependent on both the opening displacement $\boldsymbol{\chi}$ and the normal $\boldsymbol{N}$:

$$\boldsymbol{t}_0 = \boldsymbol{t}_0(\boldsymbol{\chi}, \boldsymbol{N}) \tag{46}$$

Following the framework outlined in Section 3, all geometrical operations such as the computation of the normal, $\boldsymbol{N}$, are carried out on the middle surface $\bar{S}$ with co-ordinates given by

$$\bar{\boldsymbol{y}} = \tfrac{1}{2}(\boldsymbol{y}^+ + \boldsymbol{y}^-) \tag{47}$$

Moreover, the microscale deformation is assumed to be driven by the macro-deformation $\underline{\boldsymbol{F}}$ such that the spatial co-ordinates of a particle at the microscale are

$$\boldsymbol{y} = \underline{\boldsymbol{F}}(\lambda)\boldsymbol{Y} + {}^1\boldsymbol{u} \tag{48}$$

The normal is expressed in terms of the tangent basis vectors $\boldsymbol{e}_1$ and $\boldsymbol{e}_2$ as

$$\boldsymbol{N} = \frac{\boldsymbol{e}_1 \times \boldsymbol{e}_2}{|\boldsymbol{e}_1 \times \boldsymbol{e}_2|} \tag{49}$$

where $\boldsymbol{e}_1$ and $\boldsymbol{e}_2$ are obtained using the standard isoparametric element procedure, i.e. $\boldsymbol{e}_1 = \partial\bar{\boldsymbol{y}}/\partial\boldsymbol{y}_1$, $\boldsymbol{e}_2 = \partial\bar{\boldsymbol{y}}/\partial\boldsymbol{y}_2$.

The linearized cohesive model contribution is then

$$D\boldsymbol{t}_0[\Delta^1\boldsymbol{u}^{\pm}] = \frac{\partial \boldsymbol{t}_0}{\partial \boldsymbol{\chi}} \frac{\partial \boldsymbol{\chi}}{\partial {}^1\boldsymbol{u}^{\pm}} \Delta^1\boldsymbol{u}^{\pm} + \frac{\partial \boldsymbol{t}_0}{\partial \boldsymbol{N}} \frac{\partial \boldsymbol{N}}{\partial \bar{\boldsymbol{y}}} \frac{\partial \bar{\boldsymbol{y}}}{\partial {}^1\boldsymbol{u}^{\pm}} \Delta^1\boldsymbol{u}^{\pm} \tag{50}$$

where, based on (23)–(25) and (49),

$$\begin{aligned}
\frac{\partial \boldsymbol{t}_0}{\partial \boldsymbol{\chi}} &= \frac{\psi'' \tilde{\chi} - \tilde{t}}{\tilde{\chi}^3} \hat{\boldsymbol{t}} \otimes \hat{\boldsymbol{t}} + \frac{\tilde{t}}{\tilde{\chi}} [\beta^2 \mathbf{1} + (1-\beta^2) \boldsymbol{N} \otimes \boldsymbol{N}] \\
\frac{\partial \boldsymbol{t}_0}{\partial \boldsymbol{N}} &= \frac{\psi'' \tilde{\chi} - \tilde{t}}{\tilde{\chi}^3} [\beta^2 (\boldsymbol{\chi} \cdot \boldsymbol{N})^2 \boldsymbol{N} + (1-\beta^2)(\boldsymbol{\chi} \cdot \boldsymbol{N})\boldsymbol{\chi}] \otimes \hat{\boldsymbol{t}} + \frac{\tilde{t}}{\tilde{\chi}} (1-\beta^2)[\boldsymbol{\chi} \otimes \boldsymbol{N} + (\boldsymbol{\chi} \cdot \boldsymbol{N})\mathbf{1}] \\
\frac{\partial \boldsymbol{N}}{\partial \bar{\boldsymbol{y}}} &= \frac{\mathbf{1} - (\boldsymbol{N} \otimes \boldsymbol{N})}{|\boldsymbol{e}_1 \times \boldsymbol{e}_2|} \frac{\partial (\boldsymbol{e}_1 \times \boldsymbol{e}_2)}{\partial \bar{\boldsymbol{y}}}
\end{aligned} \tag{51}$$

and

$$\psi'' \equiv \frac{\partial^2 \psi}{\partial \tilde{\chi}^2} = \frac{\partial \tilde{t}}{\partial \tilde{\chi}} = \frac{\sigma_c \, \mathrm{e}^{(-(\tilde{\chi} - \chi_c)/\chi_c)} (\chi_c - \tilde{\chi})}{\chi_c^2} \tag{52}$$

Please recall that $\mathbf{1}$ is the second-order identity tensor and $\otimes$ denotes the dyadic product. Finally, a simple calculation gives

$$\frac{\partial \boldsymbol{\chi}}{\partial {}^1\boldsymbol{u}^{\pm}} = \mathbf{1}^+ - \mathbf{1}^- \quad \text{and} \quad \frac{\partial \bar{\boldsymbol{y}}}{\partial {}^1\boldsymbol{u}^{\pm}} = \tfrac{1}{2}(\mathbf{1}^+ + \mathbf{1}^-) \tag{53}$$

5.3. Consistent linearization with respect to load multiplier λ

As mentioned earlier, the micro-history recovery procedure by Fish *et al.* [40] is used in this work to describe the response of a macroscale material point. For the sake of simplicity, the macro-deformation $\underline{\boldsymbol{F}}$ is prescribed and the loading program is parameterized by a scalar load multiplier, λ (Equation (38)).

The linearized load multiplier contributions in the residuals are

$$\begin{aligned}
D\mathscr{R}_{\boldsymbol{u}}[\Delta\lambda] = \frac{1}{|\Theta_0|} \int_{\Theta_0} \{ & [\boldsymbol{F}^{\mathrm{T}}(\nabla \delta^1\boldsymbol{u})] : \mathscr{L} : [{}^{\lambda}\boldsymbol{F}\Delta\lambda] + [(\nabla \delta^1\boldsymbol{u})^{\mathrm{T}\,\lambda}\boldsymbol{F}\Delta\lambda] : \tilde{\boldsymbol{S}} \\
& + pJ[\mathrm{tr}(\boldsymbol{F}^{-1\,\lambda}\boldsymbol{F}\Delta\lambda)\mathrm{tr}(\boldsymbol{F}^{-1}\nabla\delta^1\boldsymbol{u}) - \mathrm{tr}(\boldsymbol{F}^{-1\,\lambda}\boldsymbol{F}\Delta\lambda\boldsymbol{F}^{-1}\nabla\delta^1\boldsymbol{u})]\} \, \mathrm{d}\Theta_0 \\
& + \frac{1}{|\Theta_0|} \int_{S_0} D\boldsymbol{t}_0[\Delta\lambda] \cdot \lfloor \delta^1\boldsymbol{u} \rceil \, \mathrm{d}S_0
\end{aligned} \tag{54a}$$

$$D\mathscr{R}_p[\Delta\lambda] = \frac{1}{|\Theta_0|}\int_{\Theta_0} J\,\mathrm{tr}(\boldsymbol{F}^{-1\lambda}\boldsymbol{F}\Delta\lambda)\delta p\,\mathrm{d}\Theta_0 - \frac{1}{|\Theta_0|}\sum_{\mathrm{el}}^{\mathrm{ne}}\Lambda\int_{\Theta_0^e} J[\mathrm{tr}(\boldsymbol{F}^{-1\lambda}\boldsymbol{F}\Delta\lambda)\boldsymbol{C}^{-1}$$

$$-\boldsymbol{F}^{-1\lambda}\boldsymbol{F}\Delta\lambda\boldsymbol{C}^{-1} - \boldsymbol{C}^{-1\lambda}\boldsymbol{F}^{\mathrm{T}}\Delta\lambda\boldsymbol{F}^{-\mathrm{T}}] : [\nabla p\otimes\nabla\delta p]\,\mathrm{d}\Theta_0^e \tag{54b}$$

where ${}^{\lambda}\boldsymbol{F} \equiv \partial\boldsymbol{F}/\partial\lambda$ and the tangent pseudo-modulus $\mathscr{L}$ is given by Equation (43).

Let us now turn our attention to the linearized cohesive contributions corresponding to the load multiplier λ (Equation (54a)). The linearized load multiplier contributions in the cohesive residual are

$$D\boldsymbol{t}_0[\Delta\lambda] = \frac{\partial\boldsymbol{t}_0}{\partial\boldsymbol{\chi}}\frac{\partial\boldsymbol{\chi}}{\partial\lambda}\Delta\lambda + \frac{\partial\boldsymbol{t}_0}{\partial\boldsymbol{N}}\frac{\partial\boldsymbol{N}}{\partial\bar{\boldsymbol{y}}}\frac{\partial\bar{\boldsymbol{y}}}{\partial\lambda}\Delta\lambda \tag{55}$$

where the linearized terms $\partial\boldsymbol{t}_0/\partial\boldsymbol{\chi}$, $\partial\boldsymbol{t}_0/\partial\boldsymbol{N}$ and $\partial\boldsymbol{N}/\partial\bar{\boldsymbol{y}}$ are listed in Equation (51).

Substituting (45a) and (47) into (55), taking (48) into account and performing the corresponding partial derivatives, the linearized contribution yields

$$D\boldsymbol{t}_0[\Delta\lambda] = \pm\frac{1}{2}\frac{\partial\boldsymbol{t}_0}{\partial\boldsymbol{N}}\frac{\partial\boldsymbol{N}}{\partial\bar{\boldsymbol{y}}}{}^{\lambda}\boldsymbol{F}\boldsymbol{Y}\Delta\lambda \tag{56}$$

Please note that the linearized contributions described by (54) and (56) are in construction very similar to those relative to a configuration ${}^{1}\boldsymbol{u}$ (Equation (42)). Hence, their computation and assembly add only a relatively small computational cost and are performed at the same time the tangent stiffness matrix is constructed.

6. CONSTITUTIVE LAWS

Although the multiscale model developed in this work pertains to many reinforced elastomeric materials, we focus our attention in the examples presented hereafter on the damage evolution in an idealized solid propellant composed of ammonium perchlorate (AP) particles embedded in a rubbery binder. As mentioned earlier, to achieve high energy content, solid propellants are typically characterized by high particle volume fractions obtained through a bimodal distribution of particle sizes. The small particles have a mean diameter of about 20 μm, while that of the larger particles is in the 100–300 μm range.

As described in the introductory section, damage initiation in these materials is often associated with the debonding of the larger particles and the role of the smaller ones is primarily to stiffen the binder. In the examples presented below, we assume a 64% concentration of AP particles, with 34% of large particles. The remaining 30% of small particles is then combined with the 36% of binder to create a homogenized matrix (blend).

To capture the mechanical behaviour of the compressible AP particles and the nearly incompressible matrix, two hyperelastic material models are introduced. These models differ by the expression of the deviatoric component of their free energy density function: the functional form of the volumetric contribution is the same for both AP particles and the blend and is given by the simple relation (33).

6.1. AP particles

The deviatoric behaviour of particles is described by the following distortional component of the free density function:

$$\hat{W} = \mu \boldsymbol{E} : \boldsymbol{E} \tag{57}$$

where $\boldsymbol{E} = 1/2(\boldsymbol{C} - \boldsymbol{1})$ is the Green–Lagrange strain tensor, μ denotes the shear modulus and the deviatoric part of the second P–K stress reads

$$\tilde{\boldsymbol{S}} = 2\mu \boldsymbol{E} = \mu(\boldsymbol{C} - \boldsymbol{1}) \tag{58}$$

For this model, the Lagrangian tensor $\mathscr{C}$ entering (43) is given by

$$\mathscr{C} = 2\mu \boldsymbol{I} \tag{59}$$

where $\boldsymbol{I}$ denotes the fourth-order identity tensor.

6.2. Homogenized blend

The homogenized matrix is modelled as a nearly incompressible Neo-Hookean material with the distortional component of the free density function given by

$$\hat{W} = \tfrac{1}{2}\mu[\mathrm{tr}(\hat{\boldsymbol{C}}) - 3], \quad \hat{\boldsymbol{C}} = (\det \boldsymbol{C})^{-1/3}\boldsymbol{C} \tag{60}$$

where μ denotes the shear modulus obtained from homogenization. The deviatoric part of the second P–K stress is then given by

$$\tilde{\boldsymbol{S}} = \mu(\det \boldsymbol{C})^{-1/3}[\boldsymbol{1} - \tfrac{1}{3}\mathrm{tr}(\boldsymbol{C})\boldsymbol{C}^{-\mathrm{T}}] \tag{61}$$

The corresponding expression of the fourth-order Lagrangian tensor $\mathscr{C}$ is

$$\mathscr{C} = 2\mu(\det \boldsymbol{C})^{-1/3}[\tfrac{1}{9}\mathrm{tr}(\boldsymbol{C})\boldsymbol{C}^{-1} \otimes \boldsymbol{C}^{-1} - \tfrac{1}{3}\boldsymbol{1} \otimes \boldsymbol{C}^{-1} - \tfrac{1}{3}\boldsymbol{C}^{-1} \otimes \boldsymbol{1} + \tfrac{1}{3}\mathrm{tr}(\boldsymbol{C})\mathscr{B}] \tag{62}$$

where the fourth-order tensor $\mathscr{B}$ in indicial notation reads

$$\mathscr{B}_{IJMN} = C^{-1}_{NI} C^{-1}_{JM} \tag{63}$$

The homogenized mechanical properties of a blend, (μ, κ), are obtained by a homogenization procedure. As pointed out by Dvorak *et al.* [50], various estimates of the composite stiffness $\bar{\boldsymbol{L}}$ of any statistically homogeneous representative volume element (RVE) consisting of $r = 1, 2, \ldots, N$ phases can be written as

$$\bar{\boldsymbol{L}} = \left[\sum_{r=1}^{N} c_r (\boldsymbol{L}^* + \boldsymbol{L}_r)^{-1} \right]^{-1} - \boldsymbol{L}^* \tag{64}$$

where c_r and $\boldsymbol{L}_r$, respectively, denote the volume fraction and elastic stiffness of constituent r; $\boldsymbol{L}^* = \boldsymbol{L}_0 \mathscr{S}^{-1}(\boldsymbol{I} - \mathscr{S})$ corresponds to Hill's constraint tensor, $\boldsymbol{L}_0$ represents the stiffness of a comparison medium, $\mathscr{S}$ is the Eshelby tensor [51] and $\boldsymbol{I}$ is the identity matrix. Moreover, Walpole [52, 53] proved that (64) satisfies the Hashin–Shtrikman [3] first-order variational bounds on the actual overall elastic properties, where the bounds $\bar{\boldsymbol{L}}^+$ and $\bar{\boldsymbol{L}}^-$ on the actual stiffness $\bar{\boldsymbol{L}}$ are obtained by selecting the stiffness $\boldsymbol{L}_0$ of a comparison medium. In this work,

Table I. Mechanical properties of individual constituents. E^* denotes Young's modulus, μ represents shear modulus and ν is Poisson's ratio.

Constituent	E^* (MPa)	μ (MPa)	ν
AP particle	32.447×10^3	14.19×10^3	0.1433
Binder	2.400	0.8003	0.4995
Homogenized blend	7.393	1.2328	0.4991

Table II. Mechanical properties of binder/particle interface.

σ_c (MPa)	χ_c (μm)	G_c (J/m^2)	β
0.5	0.75	1.02	0.8

we adopt the Mori–Tanaka homogenization scheme for the blend, in which the matrix serves as the comparison medium, i.e. $\boldsymbol{L}_0 = \boldsymbol{L}_m$. This assumption provides a lower bound on the overall compliance of the composite medium.

7. EXAMPLES

We now apply the multiscale scheme to several examples involving an idealized solid propellant. All constituents are assumed to be isotropic hyperelastic solids with the free energy density described in Section 6. Only the damage response of larger particles is considered here: the stiffening effect of smaller particles on the mechanical response of the binder is modelled by considering a homogenized blend. The elastic moduli of the various components, including those of the homogenized blend, are listed in Table I. Note the very high stiffness mismatch between the particle and the blend and the near incompressibility of the blend, as quantified by Poisson's ratio approaching 1/2.

All finite element meshes are composed of four-node tetrahedral elements and have been generated using the $T3D$ generator developed by Rypl [54]. The stability parameter ω entering (36) through $\Lambda = \omega h_e^2/2\mu$ was set to one, which was shown to be adequate in finite elasticity problems [34] and no pressure oscillations were observed.

The failure behaviour of the interface between the blend and the particles is characterized by the irreversible exponential cohesive law. The cohesive parameters of the binder/particle interface adopted in the simulations presented hereafter are listed in Table II.

7.1. One-particle composite system

The first example is devoted to the damage nucleation and propagation along the particle/matrix interface in a perfectly periodic array of reinforcing particles. The SRVE is thus composed of a single particle chosen to be of spherical shape with a diameter of 174 μm. The unit cell dimensions are chosen to be $200 \times 200 \times 200$ μm, which corresponds to a particle volume fraction of about 34%. We realize that this particular choice of the SRVE is too simple to capture the complexity of actual solid propellant microstructures usually characterized by a

Table III. Finite element discretization for the one-particle unit cell. nn, ne, nce and ndof denote the number of nodes, elements, cohesive elements and degrees of freedom, respectively.

	nn	ne	nce	ndof
Periodic mesh	2450	10 584	612	8476

bimodal distribution and a high concentration of particles. However, the main goal of this work is to demonstrate the ability of the multiscale numerical framework to capture the physical complexity of decohesion process taking place along a particle/matrix interface and its effect on the stress and strain fields in the surrounding matrix.

The mesh characteristics for the one-particle periodic SRVE are listed in Table III. Three loading cases are considered characterized by the following macroscopic deformation gradients: volume preserving tension:

$$\underline{\boldsymbol{F}} = \begin{bmatrix} \dfrac{1}{(1-\lambda)^2} & 0 & 0 \\ 0 & 1-\lambda & 0 \\ 0 & 0 & 1-\lambda \end{bmatrix} \quad \text{loading case (A)} \tag{65}$$

triaxial tension-compression loading

$$\underline{\boldsymbol{F}} = \begin{bmatrix} \dfrac{1}{(1-\lambda)^2} & 0 & 0 \\ 0 & 1-\dfrac{1}{2}\lambda & 0 \\ 0 & 0 & 1-\dfrac{1}{2}\lambda \end{bmatrix} \quad \text{loading case (B)} \tag{66}$$

and simple shear

$$\underline{\boldsymbol{F}} = \begin{bmatrix} 1 & \lambda & 0 \\ 0 & 1 & 0 \\ 0 & 0 & 1 \end{bmatrix} \quad \text{loading case (C)} \tag{67}$$

where λ is the scalar load multiplier entering (38). The logarithmic strain $\underline{\varepsilon}$ was selected as the macroscopic strain measure:

$$\underline{\varepsilon} = \ln(\underline{\boldsymbol{U}}) \tag{68}$$

where $\underline{\boldsymbol{U}}$ is the macroscopic stretch tensor defined by

$$\underline{\boldsymbol{F}} = \underline{\boldsymbol{R}}\underline{\boldsymbol{U}} \tag{69}$$

with $\underline{\boldsymbol{R}}$ denoting the macroscopic rotation tensor.

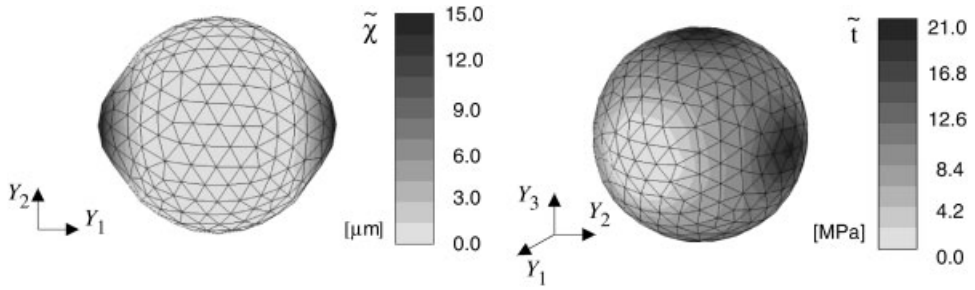

Figure 3. Effective opening displacement and effective cohesive tractions at the end of the loading process. Loading case (A).

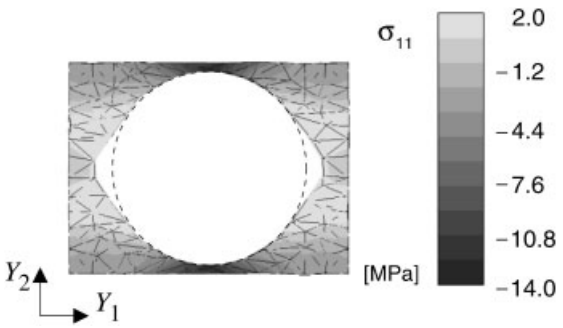

Figure 4. Normal stress σ_{11} in the blend at the middle of the unit cell at the end of the loading process. Loading case (A). Cut-off plane $\boldsymbol{Y} = \{0, 0, 100\}$.

Figure 3 shows the effective opening displacement and the effective tractions across the cohesive surface for loading case (A). As expected, progressive debonding is observed in the Y_1-direction while compressive regions are obtained in the Y_2- and Y_3-directions, respectively. This effect is due to the large lateral compressive stresses induced by the volume-preserving macroscopic deformation described by (65). The compliant blend is compressed against the hard particle, thereby preventing the propagation of the debonding crack. A lemon-like void shape is obtained as the material flows under the lateral compression in the Y_1-direction, and the void forms along the poles of the particle. This peculiar void/particle shape is shown in Figure 4, together with the σ_{11} Cauchy stress distribution. As shown there, the condition of the incompressibility of the macroscopic deformation leads to the surprising result that only a relatively small region in the unit cell experiences a tensile stress in the Y_1-direction. Equally unexpected is the computed homogenized (macroscopic) response presented in Figure 5, which indicates that the macroscopic normal Cauchy stress $\underline{\sigma}_{11}$ initially positive, as expected, becomes increasingly negative. Due to the problem symmetry and aforementioned strong lateral compression on the particle, the other two macroscopic stresses $\underline{\sigma}_{22}$ and $\underline{\sigma}_{33}$ are identical, and both increasingly negative also. These somewhat counter-intuitive results are, once again, associated with the volume preserving nature of the imposed macroscopic deformation and can be understood from a simple reasoning based on the small strain theory described in Appendix A.

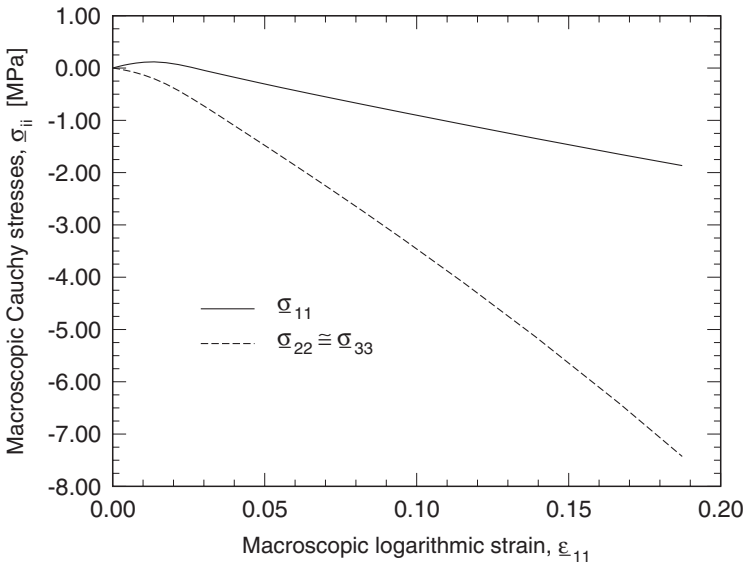

Figure 5. Macroscopic stress–strain curves for loading case (A).

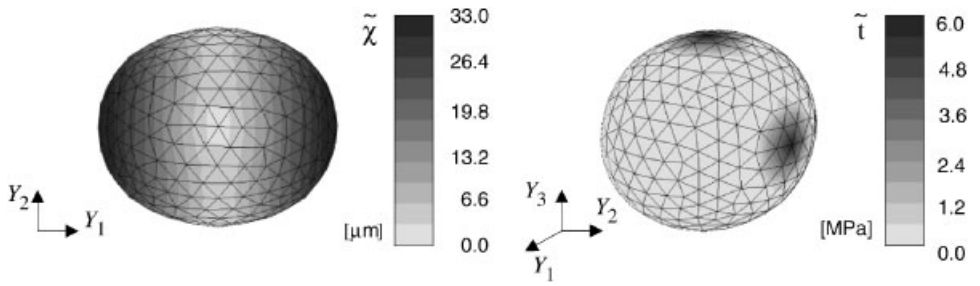

Figure 6. Effective opening displacement and effective cohesive tractions at the end of the loading process. Loading case (B).

When the isochoric assumption of the macroscopic deformation is relaxed and the lateral constraint is partially relieved, as in the second loading case (B) defined by (66), one obtains the effective opening displacement and cohesive traction distributions shown in Figure 6. As apparent there, the damage zone size is substantially larger than in case (A), with only small non-damaged regions oriented in the Y_2- and Y_3-directions still connecting the particle to the matrix. The cohesive traction distribution along the particle/matrix interface, therefore, vanishes everywhere except in those small regions. The resulting void takes the egg-like shape, shown in Figure 7, which also displays the normal σ_{11} distribution in the unit cell. As expected, most of the domain is under tensile stress in the Y_1-direction and the maximum value of the microscopic normal stress σ_{11} is obtained at the points of contact between the particle and the matrix. These stress concentrations would very likely initiate tearing of the matrix and ultimately

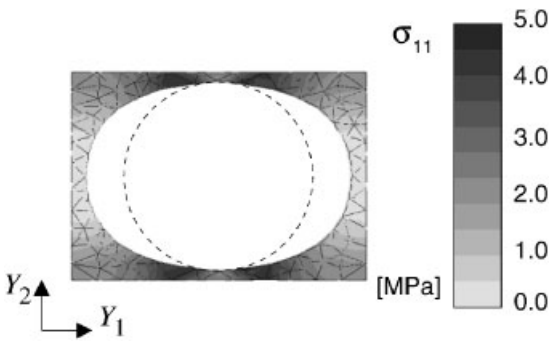

Figure 7. Normal stress σ_{11} in the blend at the middle of the unit cell at the end of the loading process. Loading case (B). Cut-off plane $\boldsymbol{Y} = \{0, 0, 100\}$.

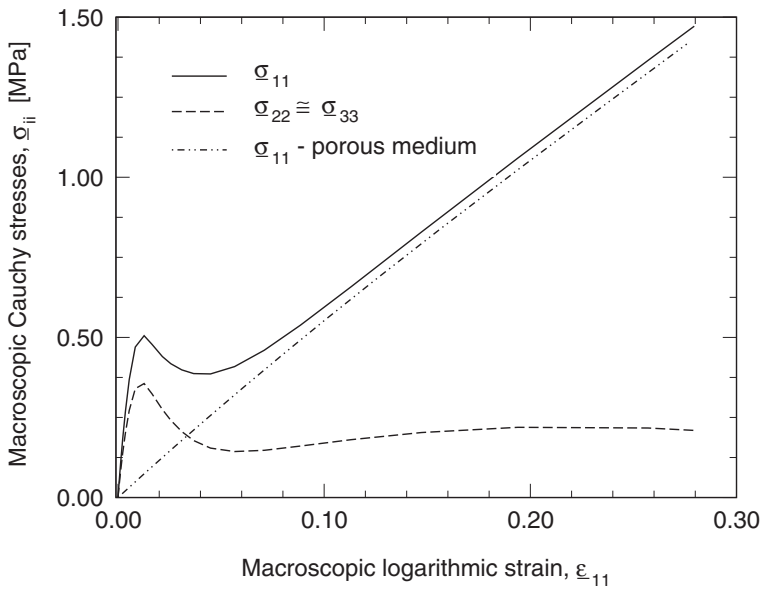

Figure 8. Macroscopic stress–strain curves for loading case (B).

lead to coalescence of the voids. The resulting macroscopic stress–strain curves, shown in Figure 8, are substantially different from those associated with loading case (A). The evolution of $\underline{\sigma}_{11}$ stress component clearly shows the initial stiff response of the composite, followed by the extensive softening associated with the particle debonding. Then comes a secondary re-hardening corresponding to the response of the damaged medium and characterized by a much lower stiffness than that of a virgin undamaged system. Due to the substantial debonding of the particle in the SRVE, the macroscopic response of the SRVE approaches a lower bound of the solution corresponding to behaviour of a fully voided matrix (denoted by the dash–dotted

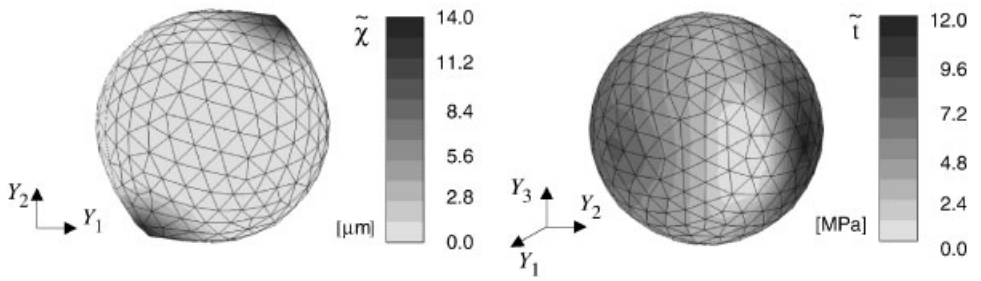

Figure 9. Effective opening displacement and effective cohesive tractions at the end of the loading process. Loading case (C).

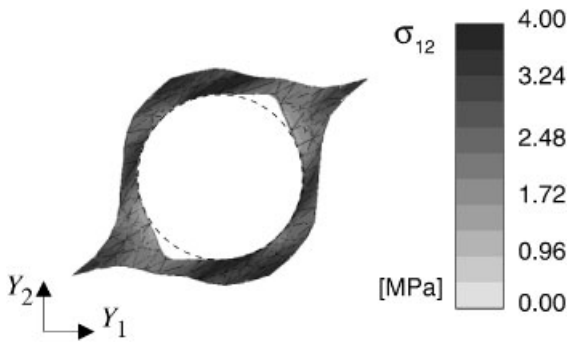

Figure 10. Shear stress σ_{12} in the blend at the middle of the unit cell at the end of the loading process. Loading case (C). Cut-off plane $\boldsymbol{Y} = \{0, 0, 100\}$.

curve in Figure 8), with the small difference due to the constraining presence of the particle that prevents the lateral deformation of the void.

The third macroscopic deformation history, (C), imposed on the micro-continuum corresponds to a plane strain simple shear loading. Please note that, while the applied macroscopic gradient (67) is 2D, the fluctuation displacement field ${}^1\boldsymbol{u}$ is fully 3D. Although the applied $\underline{\boldsymbol{F}}$ corresponds to a shear loading, the particle/matrix interface experiences both shear and tensile failure, as illustrated in Figure 9, which presents the displacement jump and cohesive traction distributions along the particle/matrix interface. Tensile failure is observed with the principal axes of the void rotated by about 55° with respect to the Y_1-direction. The characteristic shape of the void and the shear stress field in the surrounding matrix are shown in Figure 10 for a value of the loading parameter λ equal to 0.498. Note the very large shear deformation experienced by the SRVE. The macroscopic stress–strain law is displayed in Figure 11.

To conclude the discussion of the single-particle SRVE results, we present in Figure 12 the void volume fraction for the three loading cases, (A)–(C), as a function of the effective logarithmic strain. Here, the 'true' volume of voids is defined as a volume of damaged

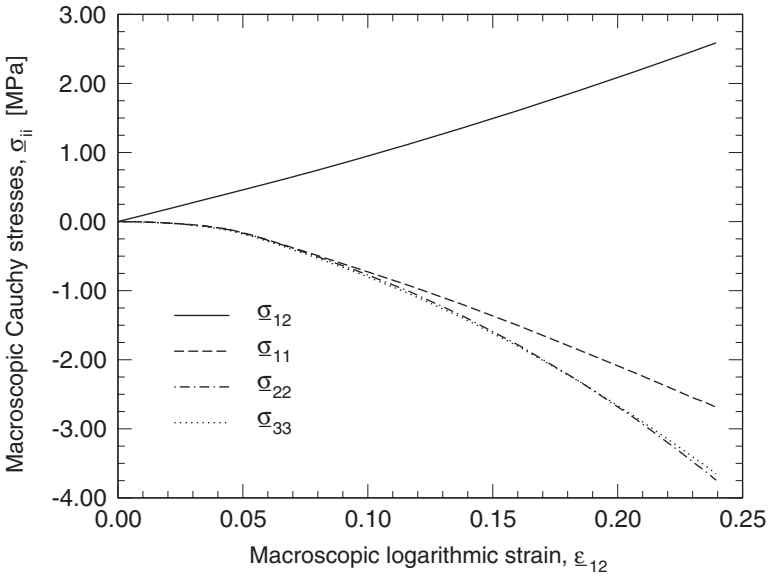

Figure 11. Macroscopic stress–strain curves for loading case (C).

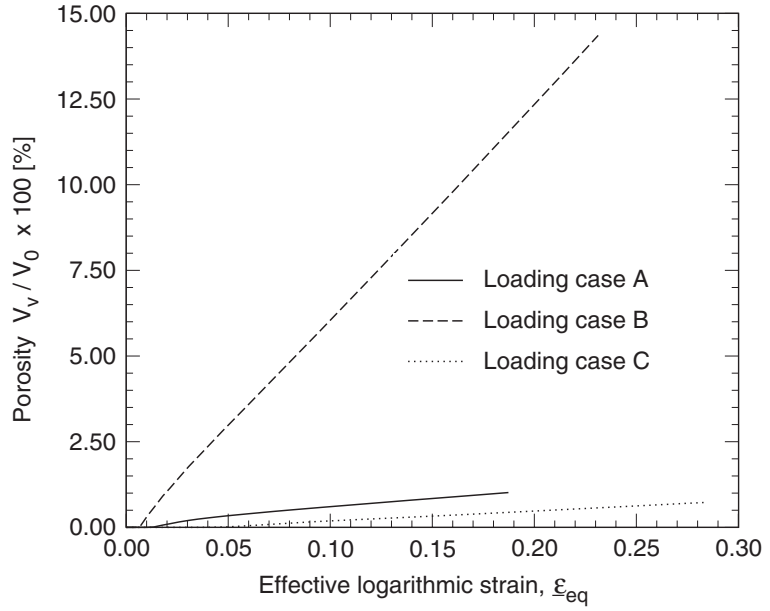

Figure 12. Evolution of porosity obtained for the three loading cases.

Table IV. Finite element discretization for the unit cell consist of four spherical particles.

	nn	ne	nce	ndof
Periodic mesh	12 921	61 536	3020	48 284

cohesive elements

$$V_v = \int_{S_0} \tilde{\chi}_n \, dS_0 \quad \text{if } \tilde{\chi} > \chi_c \quad \forall \tilde{\chi}_n > 0 \tag{70}$$

where $\tilde{\chi}_n$ denotes the normal opening across the cohesive surface. This representation of the void volume in the SRVE is different from that usually adopted in micromechanics-based studies, where the whole particles are treated as voids upon damage nucleation. Such definition would possibly lead to unrealistically large void concentrations and neglect the effect of the remaining partially bonded particles. As apparent from Figures 3, 6 and 9, the largest void formation is induced by loading history (B). For this loading program, the void volume fraction reaches almost 15% as shown in Figure 12. Much lower void volume fractions were obtained for both (A) and (C) loading histories (Figure 12), which are both volume preserving at the macroscale. For these two cases, since the blend is nearly incompressible, the volume of any void created along the particle/blend interface is balanced primarily by a reduction of the particle size. For example, in loading case (A), the maximum value of the macroscopic logarithmic strain $\underline{\varepsilon}_{11}$ is about 18.7% and the final void volume change 1.016%. The volume change in the binder is only about 0.3%.

7.2. Four-particle composite system

We now turn our attention to a second example devoted to the damage evolution in a unit cell consist of four spherical particles of diameter 174 μm. The particles are dispersed in the unit cell of dimensions $400 \times 200 \times 400$ μm with the same volume fraction to that of one-particle cell. The finite element mesh characteristics are listed in Table IV and the unit cell geometry is displayed in Figure 13. The individual particles are not organized into perfect lattice; rather, a slight centre perturbation is introduced (Table V).

When the four-particle unit cell is subjected to the same loading history (A) as the one-particle unit cell, the remarkable agreement is obtained in the macroscopic stress–strain space for the analysed portion of loading as shown in Figure 14. Although the positions of the particles are perturbed, these perturbations are relatively small and the microstructure is still very organized. The constitutive responses for the one- and four-particle unit cells therefore coalesce since these constitute a representative sampling of the material. This agreement also suggests the spatial convergence of the solution as different discretizations are used in the two unit cells.

Bifurcation is a common phenomenon in non-linear continuum mechanics and appears even in seemingly simple problems involving fairly standard constitutive models [55, 56]. Here we analyse the bifurcation of the solution obtained for two different loading histories in the four-particle unit cell problem subjected to the following macroscopic deformation gradient

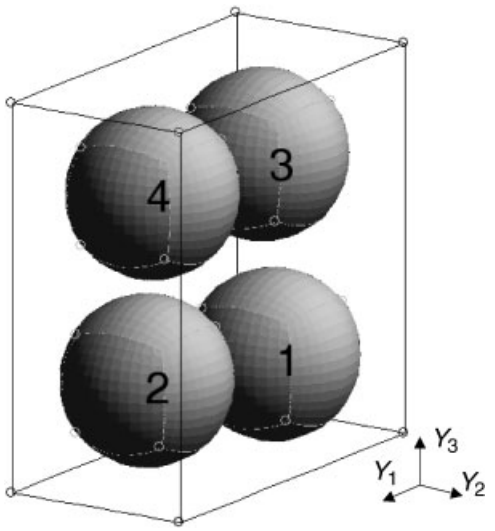

Figure 13. Geometry of four-particle unit cell.

Table V. Perturbations (given in μm) of the particle centre location for the four-particle unit cell.

Particle #	Y_1	Y_2	Y_3
1	0	+10	−10
2	+10	0	+10
3	−10	−10	−10
4	0	0	0

described by

$$\underline{\boldsymbol{F}} = \begin{bmatrix} 1 & \frac{1}{2}\lambda & 0 \\ 0 & 1 & 0 \\ 0 & 0 & 1+\lambda \end{bmatrix} \tag{71}$$

where, as before, λ denotes the scalar load multiplier used in the micro-history recovery procedure. As apparent from (71), the imposed macroscopic deformation involves a combination of tensile (in the 33-direction) and shear (in the 1–2 plane) components. When solved with the same discretization but with two different loading histories, each characterized by a different initial arc-length size, this problem leads to the bifurcation result shown in Figure 15 in terms of the macroscopic stress ($\underline{\sigma}_{33}$) versus strain ($\underline{\varepsilon}_{33}$) relation. In this work, the bifurcation points are not detected directly as this detection would require a specific numerical procedure as in Reference [55]. However, the complexity of the damage process and differences in the bifurcated solutions are important to discuss.

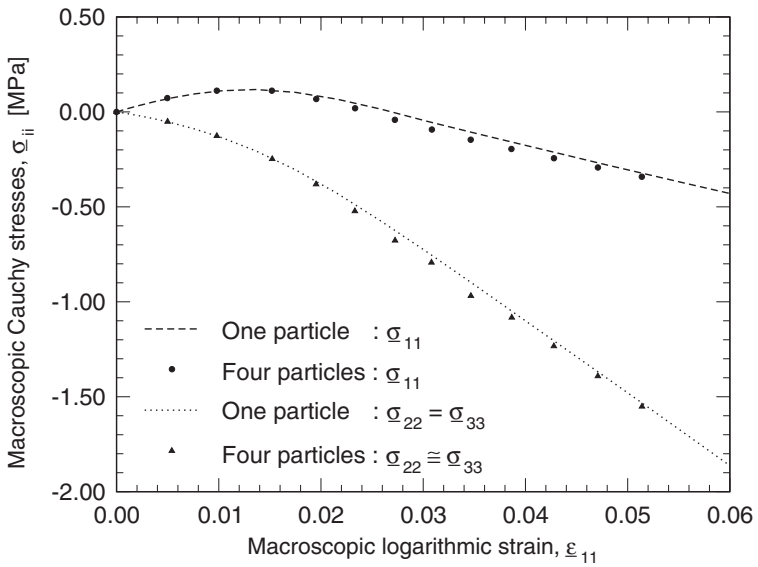

Figure 14. Comparison of macroscopic stress–strain response obtained for the one- and four-particle unit cells for loading case (A).

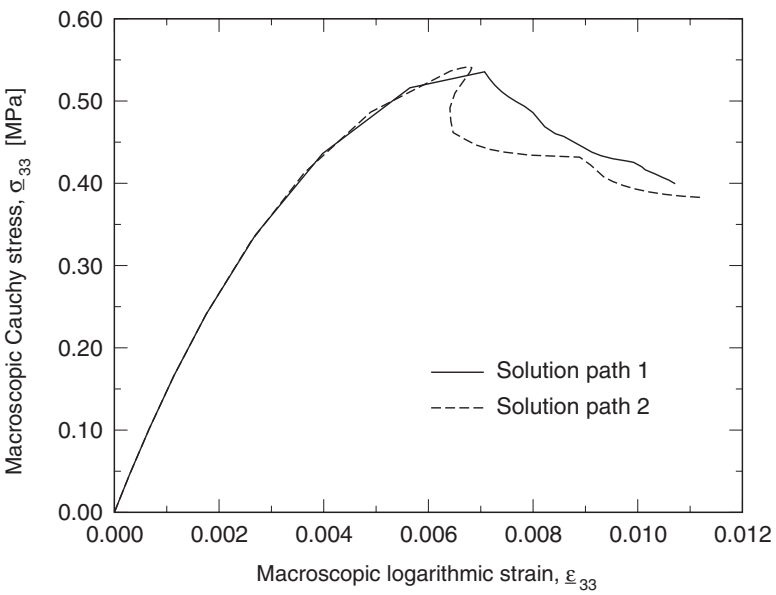

Figure 15. Macroscopic stress–strain response obtained for the four-particle unit cell.

As apparent in Figure 15, the first solution leads to a more typical non-linear stress–strain response characterized by a progressive reduction of the material stiffness that eventually leads to a softening response, for which the macroscopic stress decreases with increasing strain. This reversal takes place after a limit point is reached. At, or in the vicinity of this limit point, the macroscopic stress–strain curves for the two loading paths diverge. The second loading history yields to a snap-back response, for which failure processes taking place at the microscale initially lead to a decrease in both the macroscopic stress and strain. Then, the macroscopic constitutive response follows a softening trend that brings the material response for the second solution path back to the evolution provided by the first one. This type of result emphasizes the importance of the robustness of the numerical solver: capturing these complex events requires special numerical treatments (such as the arc-length scheme adopted in this study) as a conventional Newton algorithm typically fails.

The difference between the two macroscopic stress–strain curves can be traced to phenomena taking place at the microscale, as illustrated in Figures 16 and 17, which present the effective

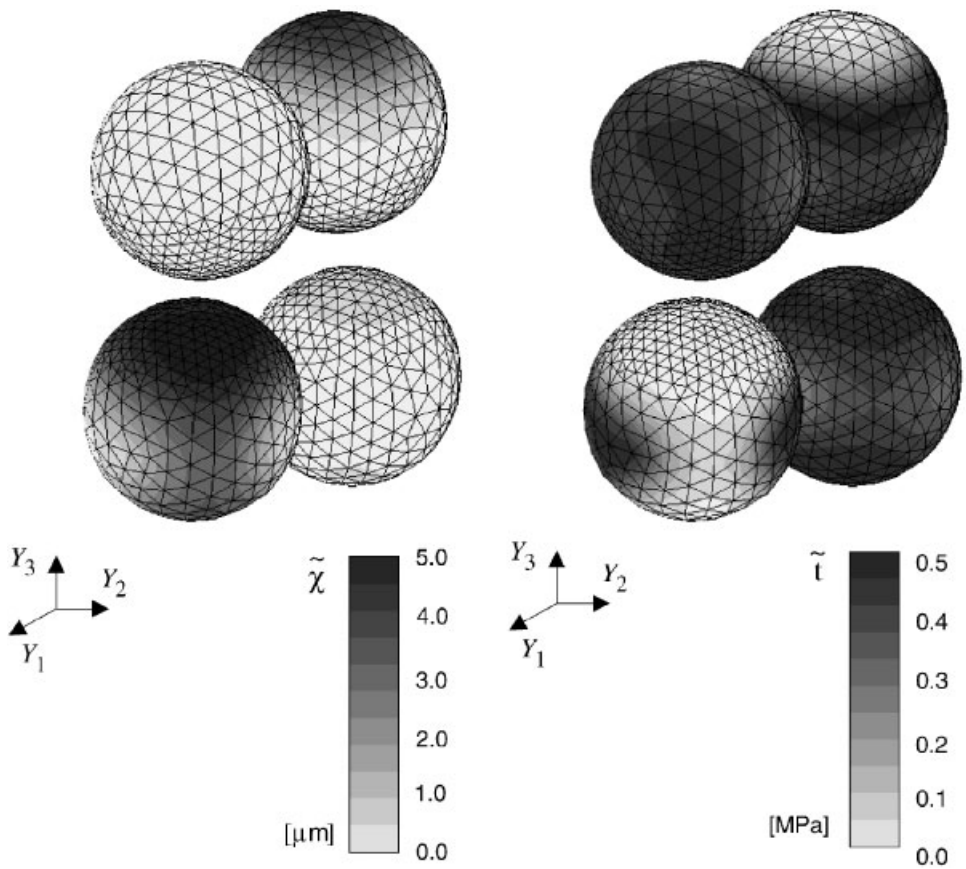

Figure 16. Effective opening displacement (left) and effective tractions (right) at the end of the loading process for solution path 1.

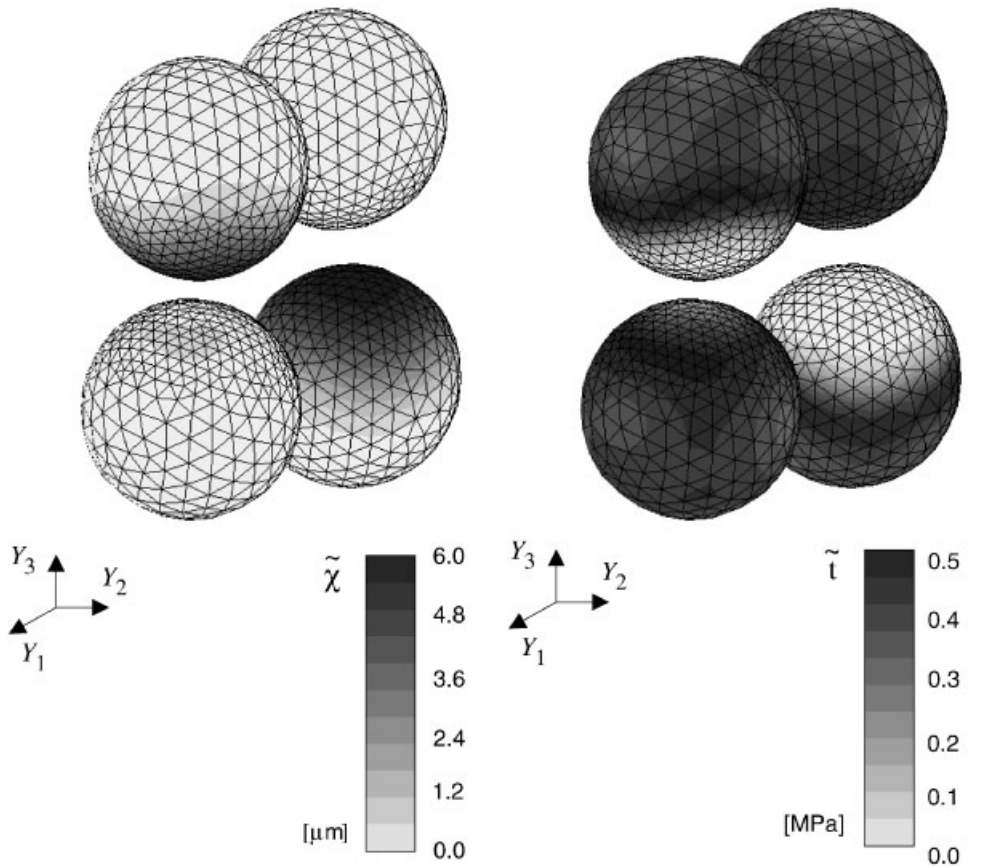

Figure 17. Effective opening displacement (left) and effective tractions (right) at the end of the loading process for solution path 2.

opening displacement and the effective traction distributions across the cohesive surface for solution paths 1 and 2, respectively. These two figures have been obtained at the end of the loading paths shown in Figure 15, i.e. for a macroscopic strain $\underline{\varepsilon_{33}}$ equal to about 1.1%. The comparison between these figures and a study of the damage evolution up to the final value of the applied macroscopic strain lead to the following observations. For the case of the first solution path (Figure 16), particle debonding is first detected at the pole of particle 2, in the vicinity of particle 4, since the small distance that separates these two particles generates a higher stress concentration. The debonding of particle 2 leads to the unloading of this matrix region, and the next debonding is observed in the vicinity of the top pole of particle 3. These debonding events take place in a relatively progressive fashion and the resulting macroscopic stress–strain curve is relatively smooth past the limit point. The situation is quite different for the second solution path, for which extensive and sudden damage is first obtained along the outer surface of particle 1 (Figure 17). This unstable debonding process corresponds to the aforementioned stress–strain curve reversal observed in Figure 15 and is followed by a plateau in the macroscopic constitutive response, where additional dewetting of particle 1 is observed

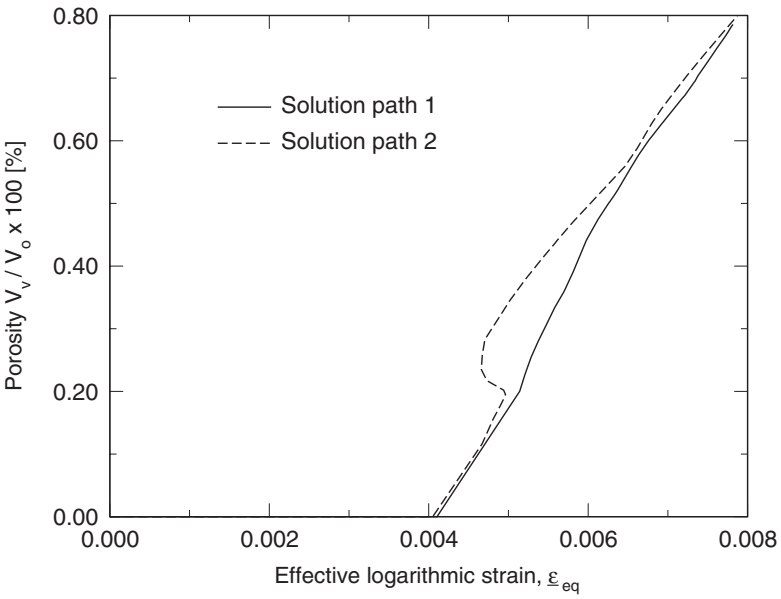

Figure 18. Evolution of porosity in the four-particle unit cell.

without increase in the resulting macroscopic stress. A second inflection point is then observed in the macroscopic stress–strain curve, which corresponds to the onset of failure at the lower pole of particle 4, leading to a macroscopic softening response similar to that obtained for the first solution path.

The difference between the two solution paths is also illustrated from the evolution of the void volume fraction shown in Figure 18. As expected, the onset of damage, corresponding to a macroscopic strain of about 0.4% is the same in both cases. Even when the material is macroscopically unloaded during the second solution path, the void volume fraction continues to grow. Due to the form of the applied macroscopic deformation (71) with a substantial part of damage associated with shear loading, the maximum value of the void volume fraction (about 0.8%) is quite small. Despite the extensive damage present in the SRVE, the overall strain is also limited (slightly over 1%). It is however important to note that, at the microscale, the strain distribution is quite heterogeneous, with maximum values exceeding 8%, as illustrated in Figure 19, which shows the effective Almansi (Eulerian) strain distribution in the matrix. This result emphasises the importance of the finite strain formulation for this class of problems. Please note that the Almansi strain measure was selected at the microscale over the Logarithmic strain used at the macroscale, since the Logarithmic strain is *local* to the material points and isocontours would not be smooth.

8. CONCLUSIONS

The mathematical theory of homogenization based on the asymptotic expansion of the displacement, deformation gradient and stress fields has been derived and used in modelling

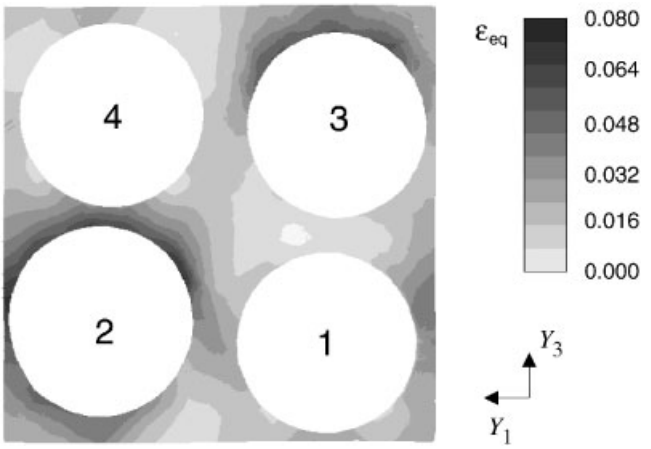

Figure 19. Microscopic effective Almansi strain, ε_{eq}, in the blend at the middle of the unit cell at the end of the loading process for solution path 1. Cut-off plane is $\boldsymbol{Y} = \{0, 100, 0\}$.

debonding (or dewetting) damage evolution in reinforced elastomers subject to finite strains. The microscale description is based on a periodic unit cell consisting of particles dispersed in a blend and incorporates the local non-homogeneous stress and deformation fields present in the unit cell during the failure of the particle/matrix interface. A novel numerical procedure is based on a stabilized Lagrangian formulation and adopts a decomposition of the pressure and displacement fields to eliminate the volumetric locking due to the nearly incompressible behaviour of a matrix. The consistent linearization of the resulting system of non-linear equations has been derived and leads to an efficient solution of the complex highly non-linear problem.

The hyperelastic behaviour of an individual constituents is defined by hyperelastic potentials and the particle matrix interface is characterized by a cohesive law. A fully implicit non-linear solver, based on the arc-length procedure is applied allowing for large loading steps.

Various examples involving simple unit cells and macroscopic deformation histories of an idealized solid propellant have been considered to study the link between the failure process taking place at the particle scale and its effect on the macroscopic stress–strain curves and the evolution of the void volume. One of these examples has illustrated the appearance of a bifurcation phenomenon associated with the progressive or sudden debonding of particles.

The emphasis of this work has been on the development of the 3D multiscale computational framework for the simulation of damage evolution in reinforced elastomers. To provide reliable predictive results, this multiscale model must allow for the simulation of a larger more representative assembly of particles, possibly of different sizes. For many materials, it should also incorporate a more complex, rate-dependent description of the matrix or blend response. These two requirements will increase the computational costs associated with the multiscale analysis, therefore requiring an efficient parallel implementation of the multiscale scheme. On the modelling side, the next step also involves the incorporation of a matrix tearing model needed to capture the initiation and propagation of matrix cracks between the voids.

APPENDIX A: LOADING CASE (A): SMALL STRAIN REASONING

To support the macroscopic results associated with case (A), let us consider the following simple linearly elastic small strain analysis of the one-particle unit cell with $Y_2 \equiv Y_3$ symmetry subjected to the volume preserving macroscopic strain field $\underline{\varepsilon}_{22} \equiv \underline{\varepsilon}_{33} = -\underline{\varepsilon}_{11}/2$. The macroscopic constitutive equations for normal stress components are

$$\begin{aligned} \underline{\sigma}_{11} &= \underline{L}_{11}\underline{\varepsilon}_{11} + \underline{L}_{12}\underline{\varepsilon}_{22} + \underline{L}_{13}\underline{\varepsilon}_{33} \\ \underline{\sigma}_{22} &= \underline{L}_{12}\underline{\varepsilon}_{11} + \underline{L}_{22}\underline{\varepsilon}_{22} + \underline{L}_{23}\underline{\varepsilon}_{33} \\ \underline{\sigma}_{33} &= \underline{L}_{13}\underline{\varepsilon}_{11} + \underline{L}_{23}\underline{\varepsilon}_{22} + \underline{L}_{33}\underline{\varepsilon}_{33} \end{aligned} \tag{A1}$$

where $\underline{L}_{ij}$ denotes the unknown damaged macroscopic moduli (in matrix notation).

Let us first consider the special case of a composite with no internal damage. The response of such a system would correspond to the upper bound of the solution. In this case, the macro-continuum has the cubic symmetry

$$\begin{aligned} \underline{L}_{11} &\equiv \underline{L}_{22} \equiv \underline{L}_{33} \\ \underline{L}_{12} &\equiv \underline{L}_{13} \equiv \underline{L}_{23} \end{aligned} \tag{A2}$$

and the macroscopic stresses are expressed as

$$\begin{aligned} \underline{\sigma}_{11} &= [\underline{L}_{11} - \underline{L}_{12}]\underline{\varepsilon}_{11} \\ \underline{\sigma}_{22} &\equiv \underline{\sigma}_{33} = -\tfrac{1}{2}\underline{\sigma}_{11} \\ \underline{\sigma}_{\mathrm{eq}} &= \tfrac{3}{2}|\underline{\sigma}_{11}| \end{aligned} \tag{A3}$$

where $\underline{\sigma}_{\mathrm{eq}}$ denotes the von Mises effective stress. In the presence of damage with $Y_2 \equiv Y_3$ symmetry, we have

$$\begin{aligned} \underline{L}_{11} &\neq (\underline{L}_{22} \equiv \underline{L}_{33}) \\ \underline{L}_{12} &\equiv \underline{L}_{13} \neq \underline{L}_{23} \end{aligned} \tag{A4}$$

The macroscopic stress–strain response becomes

$$\begin{aligned} \underline{\sigma}_{11} &= [\underline{L}_{11} - \underline{L}_{12}]\underline{\varepsilon}_{11} \\ \underline{\sigma}_{22} &\equiv \underline{\sigma}_{33} = [\underline{L}_{12} - \tfrac{1}{2}(\underline{L}_{22} + \underline{L}_{23})]\underline{\varepsilon}_{11} \end{aligned} \tag{A5}$$

For the sake of simplicity, let us consider a model material with exponentially decaying elastic constants $\underline{L}_{11} = \underline{L}^*_{11}\mathrm{e}^{(-\underline{\varepsilon}_{11})}$ and $\underline{L}_{12} = \underline{L}^*_{12}\mathrm{e}^{(-0.5\underline{\varepsilon}_{11})}$. Such softening can be expected since, for the type of damage considered in this work, damage degradation in $_{11}$ direction is more pronounced than in $_{12}$ direction. Using the virgin (non-damaged) material properties L^*_{ij} listed in Table AI, we obtain the constitutive curves shown in Figure A1, which are similar to those displayed in Figure 5.

Table AI. Mechanical properties of a model composite.

Stiffness	$\underline{L}^*_{11} \equiv \underline{L}^*_{22} \equiv \underline{L}^*_{33}$ (MPa)	$\underline{L}^*_{12} \equiv \underline{L}^*_{13} \equiv \underline{L}^*_{23}$ (MPa)
Modelled material	303	292

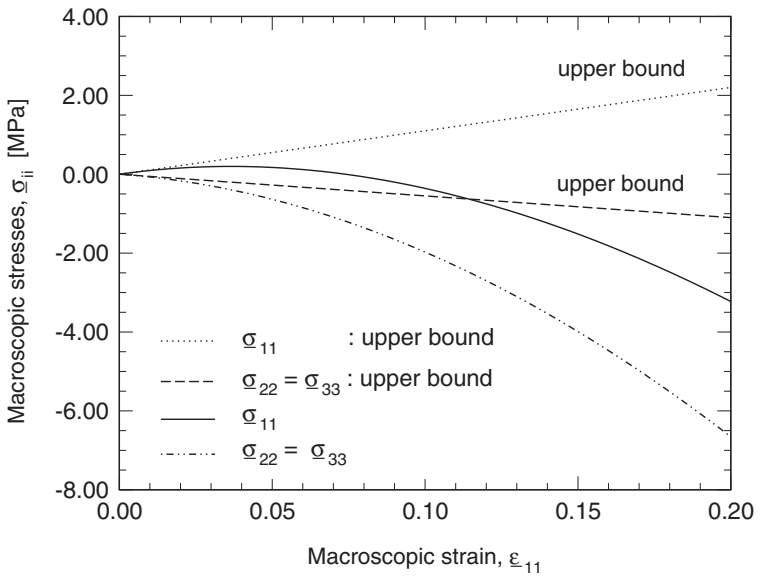

Figure A1. Macroscopic stress–strain curves for a model material subjected to loading case (A).

ACKNOWLEDGEMENTS

The authors gratefully acknowledge support from the Center for Simulation of Advanced Rockets (CSAR) at the University of Illinois, Urbana-Champaign. Research at CSAR is funded by the U.S. Department of Energy as a part of its Advanced Simulation and Computing (ASC) program under contract number B341494.

REFERENCES

1. Hill R. On macroscopic effects of heterogeneity in elastoplastic media at finite strain. *Mathematical Proceedings of the Cambridge Philosophical Society* 1984; **95**:481–494.
2. Hill R. On the micro-to-macro transition in constitutive analyses of elastoplastic response at finite strain. *Mathematical Proceedings of the Cambridge Philosophical Society* 1985; **98**:579–590.
3. Hashin Z, Shtrikman S. On some variational principles in anisotropic and nonhomogeneous elasticity. *Journal of the Mechanics and Physics of Solids* 1962; **10**:335–342.
4. Willis JR. The structure of overall constitutive relations for a class of nonlinear composites. *IMA Journal of Applied Mathematics* 1989; **43**:231–242.
5. Matouš K. Damage evolution in particulate composite materials. *International Journal of Solids and Structures* 2003; **40**:1489–1503.
6. Fish J, Yu Q. Multiscale damage modeling for composite materials: theory and computational framework. *International Journal for Numerical Methods in Engineering* 2001; **52**(1–2):161–192.

7. Guedes JM, Kikuchi N. Preprocessing and postprocessing for materials based on the homogenization method with adaptive finite element methods. *Computer Methods in Applied Mechanics and Engineering* 1990; **83**(1–2):143–198.
8. Michel JC, Moulinec P, Suquet P. Effective properties of composite materials with periodic microstructure: a computational approach. *Computer Methods in Applied Mechanics and Engineering* 1999; **172**:109–143.
9. Miehe Ch, Schröder J, Becker M. Computational homogenization analysis in finite elasticity: material and structural instabilities on the micro- and macro-scales of periodic composites and their interaction. *Computer Methods in Applied Mechanics and Engineering* 2000; **191**:4971–5005.
10. Kouznetsova V, Geers MGD, Brekelmans WAM. Multi-scale constitutive modelling of heterogeneous materials with a gradient-enhanced computational homogenization scheme. *International Journal for Numerical Methods in Engineering* 2002; **54**:1235–1260.
11. Gosh S, Lee K, Raghavan P. A multi-level computational model for multi-scale damage analysis in composite and porous materials. *International Journal of Solids and Structures* 2001; **38**:2335–2385.
12. Garikipati K, Hughes TJR. A variational multiscale approach to strain localization—formulation for multidimensional problems. *Computer Methods in Applied Mechanics and Engineering* 2000; **188**:39–60.
13. Strouboulis T, Zhang L, Babuska I. p-version of the generalized FEM using mash-based handbooks with 17 applications to multiscale problems. *International Journal for Numerical Methods in Engineering* 2004; **60**(10):1639–1672.
14. Fish J, Chen W. RVE based multilevel method for periodic heterogeneous media with strong scale mixing. *Journal of Applied Mathematics* 2003; **46**:87–106.
15. Bencher CD, Dauskardt RH, Ritchie RO. Microstructural damage and fracture processes in a composite solid rocket propellant. *Journal of Spacecraft and Rockets* 1995; **32**(2):328–334.
16. Rae PJ, Goldrein TH, Palmer SJP, Field JE, Lewis AL. Quasi-static studies of the deformation and failure of β-HMX based polymer bonded explosives. *Proceedings of the Royal Society of London A* 2002; **458**:743–762.
17. Bergstrom J, Boyce MC. Constitutive modeling of the large strain time-dependent behavior of elastomers. *Journal of the Mechanics and Physics of Solids* 1998; **46**(5):931–954.
18. Drozdov AK, Dorfmann A. A micro-mechanical model for the response of filled elastomers at finite strains. *International Journal of Plasticity* 2003; **19**:1037–1067.
19. Farris RJ. The character of the stress–strain function for highly filled elastomers. *Transactions of the Society of Rheology* 1968; **12**:303–314.
20. Schapery RA. Nonlinear viscoelastic and viscoplastic constitutive equations with growing damage. *International Journal of Fracture* 1999; **97**:33–66.
21. Ha K, Schapery RA. A three-dimensional viscoelastic constitutive model for particulate composites with growing damage and its experimental validation. *International Journal of Solids and Structures* 1998; **26**(27):3497–3517.
22. Simo JC. On a fully three-dimensional finite-strain viscoelastic damage model: formulation and computational aspects. *Computer Methods in Applied Mechanics and Engineering* 1987; **60**:153–173.
23. Ravichandran G, Liu CT. Modeling constitutive behavior of particulate composites undergoing damage. *International Journal of Solids and Structures* 1995; **32**:979–990.
24. Kwon YW, Liu CT. Effect of particle distribution on initial cracks forming from notch tips in composites with hard particles embedded in a soft matrix. *Composites B* 2001; **32**:199–208.
25. Tan H, Huang Y, Liu C, Geubelle PH. The Mori–Tanaka method for composite materials with nonlinear interface debonding. *International Journal of Plasticity* 2005; **21**(10):1890–1918.
26. Dorfmann A, Ogden RW. A constitutive model for the Mullins effect with permanent set in particle-reinforced rubber. *International Journal of Solids and Structures* 2004; **41**:1855–1878.
27. Kaliske M, Rothert H. Constitutive approach to rate-independent properties of filled elastomers. *International Journal of Solids and Structures* 1998; **35**(17):2057–2071.
28. Miehe C, Keck J. Superimposed finite elastic-viscoelastic-plastoelastic stress response with damage in filled rubbery polymers. Experiments, modelling and algorithmic implementation. *Journal of the Mechanics and Physics of Solids* 2000; **48**:323–365.
29. Brezzi F, Fortin M. *Mixed and Hybrid Finite Element Methods*. Springer: New York, 1991.
30. Matouš K, Maniatty AM. Finite element formulation for modeling large deformations in elasto-viscoplastic polycrystals. *International Journal for Numerical Methods in Engineering* 2004; **60**:2313–2333.
31. Simo JC, Taylor RL, Pister KS. Variational and projection methods for the volume constraint in finite deformation elasto-plasticity. *Computer Methods in Applied Mechanics and Engineering* 1985; **51**:177–208.

32. Brink U, Stein E. On some mixed finite element methods for incompressible and nearly incompressible finite elasticity. *Computational Mechanics* 1996; **19**:105–119.
33. Hughes TJR, Franka LP, Balestra M. A new finite element formulation for computational fluid dynamics: V. Circumventing the Babuška–Brezzi condition: a stable Petrov–Galerkin formulation of the Stokes problem accommodating equal-order interpolations. *Computer Methods in Applied Mechanics and Engineering* 1986; **59**:85–99.
34. Klaas O, Maniatty A, Shephard MS. A stabilized mixed finite element method for finite elasticity. Formulation for linear displacement and pressure interpolation *Computer Methods in Applied Mechanics and Engineering* 1999; **180**:65–79.
35. Oñate E, Rojek J, Taylor RL, Zienkiewicz OC. Finite calculus formulation for incompressible solids using linear triangles and tetrahedra. *International Journal for Numerical Methods in Engineering* 2004; **59**: 1473–1500.
36. Zhong AX, Knauss WG. Analysis of interfacial failure in particle-filled elastomers. *Journal of Engineering Materials and Technology* 1997; **119**:198–204.
37. Zhong AX, Knauss WG. Effects of particle interaction and size variation on damage evolution in filled elastomers. *Mechanics of Composite Materials and Structures* 2000; **7**:35–53.
38. Geubelle PH, Baylor JS. Impact-induced delamination of composites: a 2D simulation. *Composites Part B* 1998; **29B**:589–602.
39. Ortiz M, Pandolfi A. Finite-deformation irreversible cohesive element for three-dimensional. Crack-propagation analysis. *International Journal for Numerical Methods in Engineering* 1999; **44**:1267–1282.
40. Fish J, Shek K, Pandheeradi M, Shephard MS. Computational plasticity for composite structures based on mathematical homogenization: theory and practice. *Computer Methods in Applied Mechanics and Engineering* 1997; **148**:53–73.
41. Wells GN, Sluys LJ. A new method for modelling cohesive cracks using finite elements. *International Journal for Numerical Methods in Engineering* 2001; **50**:2667–2682.
42. Lubliner J. On thermodynamic foundations of non-linear solid mechanics. *International Journal of Non-Linear Mechanics* 1972; **7**:237–254.
43. Lubliner J. On the structure of the rate equations of materials with internal variables. *Acta Mechanica* 1973; **17**:109–119.
44. Roy YA, Dodds RH. Simulation of ductile crack growth in thin aluminum panels using 3-D surface cohesive elements. *International Journal of Fracture* 2001; **110**:21–45.
45. Xu XP, Needleman A. A numerical study of dynamic crack growth in brittle solids. *International Journal of Solids and Structures* 1994; **84**:769–788.
46. Simo JC, Wriggers P, Schweizerhof KH, Taylor RL. Finite deformation post-buckling analysis involving inelasticity and contact constraints. *International Journal for Numerical Methods in Engineering* 1986; **23**:779–800.
47. Bonet J, Wood RD. *Nonlinear Continuum Mechanics for Finite Element Analysis*. Cambridge University Press: New York, 1997.
48. Simo JC, Taylor RL. Consistent tangent operators for rate-independent elastoplasticity. *Computer Methods in Applied Mechanics and Engineering* 1985; **48**:101–118.
49. Davis TA, Duff IS. A combined unifrontal/multifrontal method for unsymmetric sparse matrices. *ACM Transactions on Mathematical Software* 1999; **25**(1):1–19. UMFPACK page. http://www.cise.ufl.edu/research/sparse/umfpack/
50. Dvorak GJ, Srinivas MV. New estimates of overall properties of heterogeneous solids. *Journal of the Mechanics and Physics of Solids* 1999; **47**:899–920.
51. Eshelby JD. The determination of the elastic field of an ellipsoidal inclusion and related problems. *Proceedings of the Royal Society of London* 1957; **A241**:376–396.
52. Walpole LJ. On bounds for the overall elastic moduli of inhomogeneous system I. *Journal of the Mechanics and Physics of Solids* 1969; **14**:151–162.
53. Walpole LJ. On bounds for the overall elastic moduli of inhomogeneous system II. *Journal of the Mechanics and Physics of Solids* 1969; **14**:289–301.
54. Rypl D. Sequential and parallel generation of unstructured 3D meshes. *Ph.D. Thesis*, *CTU Reports*, *No. 2*, vol. 3. Czech Technical University: Prague, 1998. T3d page; http://ksm.fsv.cvut.cz/~dr/t3d.html
55. Wriggers P, Simo JC. A general procedure for the direct computation of turning and bifurcation points. *International Journal for Numerical Methods in Engineering* 1990; **30**:155–176.
56. Marsden JE, Hughes TJR. *Mathematical Foundations of Elasticity*. Prentice-Hall: Englewood Cliffs, NJ, 1983.

